



Universiteit Gent
Faculteit Wetenschappen
Vakgroep Fysica en Sterrenkunde

² No title yet

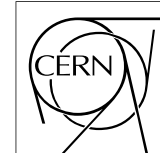
³ No sub-title neither, obviously...

⁴ Alexis Fagot

⁵



Thesis to obtain the degree of
Doctor of Philosophy in Physics
Academic years 2012-2017



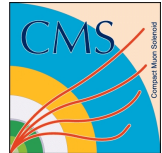


Universiteit Gent
Faculteit Wetenschappen
Vakgroep Fysica en Sterrenkunde

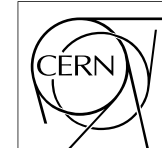
Promotoren: Dr. Michael Tytgat
Prof. Dr. Dirk Ryckbosch

Universiteit Gent
Faculteit Wetenschappen
Vakgroep Fysica en Sterrenkunde
Proeftuinstraat 86, B-9000 Gent, België
Tel.: +32 9 264.65.28
Fax.: +32 9 264.66.97

17



Thesis to obtain the degree of
Doctor of Philosophy in Physics
Academic years 2012-2017



Acknowledgements

¹⁹ Ici on remerciera tous les gens que j'ai pu croiser durant cette aventure et qui m'ont
²⁰ permis de passer un bon moment

²¹ *Gent, ici la super date de la mort qui tue de la fin d'écriture*
²² *Alexis Fagot*

Table of Contents

23

24	Acknowledgements	i
25	Nederlandse samenvatting	xix
26	English summary	xxi
27	1 Introduction	1-1
28	1.1 A story of High Energy Physics	1-1
29	1.2 Organisation of this study	1-1
30	2 Investigating the TeV scale	2-1
31	2.1 The Standard Model of Particle Physics	2-1
32	2.2 The Large Hadron Collider and the Compact Muon Solenoid	2-1
33	2.3 Muon Phase-II Upgrade	2-1
34	3 Amplification processes in gaseous detectors	3-1
35	3.1 Signal formation	3-1
36	3.2 Gas transport parameters	3-1
37	4 Resistive Plate Chambers	4-1
38	4.1 Principle	4-1
39	4.2 Rate capability of Resistive Plate Chambers	4-1
40	4.3 High time resolution	4-1
41	4.4 Resistive Plate Chambers at CMS	4-1
42	4.4.1 Overview	4-1
43	4.4.2 The present RPC system	4-2
44	4.4.3 Pulse processing of CMS RPCs	4-3
45	5 Longevity studies and Consolidation of the present CMS RPC subsystem	5-1
46	5.1 Testing detectors under extreme conditions	5-1
47	5.1.1 The Gamma Irradiation Facilities	5-3
48	5.1.1.1 GIF	5-3
49	5.1.1.2 GIF++	5-5
50	5.2 Preliminary tests at GIF	5-8
51	5.2.1 Resistive Plate Chamber test setup	5-8

53	5.2.2	Data Acquisition	5-10
54	5.2.3	Geometrical acceptance of the setup layout to cosmic muons	5-10
55	5.2.3.1	Description of the simulation layout	5-11
56	5.2.3.2	Simulation procedure	5-13
57	5.2.3.3	Results	5-14
58	5.2.4	Photon flux at GIF	5-15
59	5.2.4.1	Expectations from simulations	5-15
60	5.2.4.2	Dose measurements	5-19
61	5.2.5	Results and discussions	5-20
62	5.3	Longevity tests at GIF++	5-21
63	5.3.1	Description of the Data Acquisition	5-25
64	5.3.2	RPC current, environmental and operation parameter mon- itoring	5-26
65	5.3.3	Measurement procedure	5-27
66	5.3.4	Longevity studies results	5-27
68	6	Investigation on high rate RPCs	6-1
69	6.1	Rate limitations and ageing of RPCs	6-1
70	6.1.1	Low resistivity electrodes	6-1
71	6.1.2	Low noise front-end electronics	6-1
72	6.2	Construction of prototypes	6-1
73	6.3	Results and discussions	6-1
74	7	Conclusions and outlooks	7-1
75	7.1	Conclusions	7-1
76	7.2	Outlooks	7-1
77	A	A data acquisition software for CAEN VME TDCs	A-1
78	A.1	GIF++ DAQ file tree	A-1
79	A.2	Usage of the DAQ	A-2
80	A.3	Description of the readout setup	A-3
81	A.4	Data read-out	A-4
82	A.4.1	V1190A TDCs	A-4
83	A.4.2	DataReader	A-7
84	A.5	Communications	A-11
85	A.5.1	V1718 USB Bridge	A-11
86	A.5.2	Configuration file	A-12
87	A.5.3	WebDCS/DAQ intercommunication	A-14
88	A.5.4	Example of inter-process communication cycle	A-15
89	A.6	DAQ algorithm overview	A-17
90	A.7	Software export	A-17
91	B	Details on the online analysis package	B-1
92	B.1	Introduction	B-1

93	C Structure of the hybrid simulation software	C-1
94	C.1 Introduction	C-1

List of Figures

95

96	2.1	Absorbed dose in the CMS cavern after an integrated luminosity of 3000 fb. R is the transverse distance from the beamline and Z is the distance along the beamline from the Interaction Point at Z=0.	2-2
97			
98			
99	2.2	A quadrant of the muon system, showing DTs (yellow), RPCs (light blue), and CSCs (green). The locations of new forward muon detectors for Phase-II are contained within the dashed box and indicated in red for GEM stations (ME0, GE1/1, and GE2/1) and dark blue for improved RPC (iRPC) stations (RE3/1 and RE4/1).	2-3
100			
101			
102			
103			
104	2.3	RMS of the multiple scattering displacement as a function of muon p_T for the proposed forward muon stations. All of the electromag- netic processes such as bremsstrahlung and magnetic field effect are included in the simulation.	2-4
105			
106			
107			
108	4.1	Signals from the RPC strips are shaped by the FEE described on Figure 4.1a. Output LVDS signals are then read-out by a TDC module connected to a computer or converted into NIM and sent to scalers. Figure 4.1b describes how these converted signals are put in coincidence with the trigger.	4-4
109			
110			
111			
112			
113	4.2	Description of the principle of a CFD. A comparison of threshold triggering (left) and constant fraction triggering (right) is shown in Figure 4.2a. Constant fraction triggering is obtained thanks to zero-crossing technique as explained in Figure 4.2b. The signal arriving at the input of the CFD is split into three components. A first one is delayed and connected to the inverting input of a first comparator. A second component is connected to the noninverting input of this first comparator. A third component is connected to the noninverting input of another comparator along with a thresh- old value connected to the inverting input. Finally, the output of both comparators is fed through an AND gate.	4-5
114			
115			
116			
117			
118			
119			
120			
121			
122			
123			
124	5.1	(5.1a) Extrapolation from 2016 data of single hit rate per unit area in the barrel region. (5.1b) Extrapolation from 2016 data of single hit rate per unit area in the endcap region.	5-2
125			
126			

127	5.2	Background Fluka simulation compared to 2016 Data at $L = 10^{34} \text{ cm}^{-2} \cdot \text{s}^{-1}$ in the fourth endcap disk region. A mismatch in between simulation and data can be observed. [To be understood.]	5-3
130	5.3	Layout of the test beam zone called X5c GIF at CERN. Photons from the radioactive source produce a sustained high rate of random hits over the whole area. The zone is surrounded by 8 m high and 80 cm thick concrete walls. Access is possible through three entry points. Two access doors for personnel and one large gate for material. A crane allows installation of heavy equipment in the area.	5-4
137	5.4	^{137}Cs decays by β^- emission to the ground state of ^{137}Ba (BR = 5.64%) and via the 662 keV isomeric level of ^{137}Ba (BR = 94.36%) whose half-life is 2.55 min.	5-5
140	5.5	Floor plan of the GIF++ facility. When the facility downstream of the GIF++ takes electron beam, a beam pipe is installed along the beam line (z-axis). The irradiator can be displaced laterally (its center moves from $x = 0.65$ m to 2.15 m), to increase the distance to the beam pipe.	5-6
145	5.6	Simulated unattenuated current of photons in the xz plane (Figure 5.6a) and yz plane (Figure 5.6b) through the source at $x = 0.65$ m and $y = 0$ m. With angular correction filters, the current of 662 keV photons is made uniform in xy planes.	5-7
149	5.7	Description of the RPC setup. Dimensions are given in mm. A tent containing RPCs is placed at 1720 mm from the source container. The source is situated in the center of the container. RE-4-2-BARC-161 chamber is 160 mm inside the tent. This way, the distance between the source and the chambers plan is 2060 mm. Figure 5.7a provides a side view of the setup in the xz plane while Figure 5.7b shows a top view in the yz plane.	5-8
156	5.8	RE-4-2-BARC-161 chamber is inside the tent as described in Figure 5.7. In the top right, the two scintillators used as trigger can be seen. This trigger system has an inclination of 10° relative to horizontal and is placed above half-partition B2 of the RPCs. PMT electronics are shielded thanks to lead blocks placed in order to protect them without stopping photons from going through the scintillators and the chamber.	5-9

163	5.9 Hit distributions over all 3 partitions of RE-4-2-BARC-161 chamber is showed on these plots. Top, middle and bottom figures respectively correspond to partitions A, B, and C. These plots show that some events still occur in other half-partitions than B2, which corresponds to strips 49 to 64, in front of which the trigger is placed, contributing to the inefficiency of detection of cosmic muons.	5-10
173	5.10 Results are derived from data taken on half-partition B2 only. On the 18 th of June 2014, data has been taken on chamber RE-2-BARC-161 at building 904 (Prevessin Site) with cosmic muons providing us a reference efficiency plateau of $(97.54 \pm 0.15)\%$ represented by a black curve. A similar measurement has been done at GIF on the 21 st of July with the same chamber giving a plateau of $(78.52 \pm 0.94)\%$ represented by a red curve.	5-11
180	5.11 Representation of the layout used for the simulations of the test setup. The RPC is represented as a yellow trapezoid while the two scintillators as blue cuboids looking at the sky. A green plane corresponds to the muon generation plane within the simulation. Figure 5.7a shows a global view of the simulated setup. Figure 5.7b shows a zommed view that allows to see the 2 scintillators as well as the full RPC plane.	5-12
187	5.12 γ flux $F(D)$ is plot using values from table 5.1. As expected, the plot shows similar attenuation behaviours with increasing distance for each absorption factors.	5-15
190	5.13 Figure 5.13a shows the linear approximation fit done via formulae 5.7 on data from table 5.2. Figure 5.13b shows a comparison of this model with the simulated flux using a and b given in figure 5.13a in formulae 5.4 and the reference value $D_0 = 50\text{cm}$ and the associated flux for each absorption factor F_0^{ABS} from table 5.1	5-17
196	5.14 Dose measurements has been done in a plane corresponding to the tents front side. This plan is 1900 mm away from the source. As explained in the first chapter, a lens-shaped lead filter provides a uniform photon flux in the vertical plan orthogonal to the beam direction. If the second line of measured fluxes is not taken into account because of lower values due to experimental equipments in the way between the source and the tent, the uniformity of the flux is well showed by the results.	5-19
204	5.15	5-20

205	5.16 Evolution of the maximum efficiency for RE2 (5.16a) and RE4	
206	(5.16b) chambers with increasing extrapolated γ rate per unit area	
207	at working point. Both irradiated (blue) and non irradiated (red)	
208	chambers are shown.	5-22
209	5.17 Evolution of the working point for RE2 (5.17a) and RE4 (5.17b)	
210	with increasing extrapolated γ rate per unit area at working point.	
211	Both irradiated (blue) and non irradiated (red) chambers are shown. 5-23	
212	5.18 Evolution of the maximum efficiency at HL-LHC conditions, i.e.	
213	a background hit rate per unit area of 300 Hz/cm ² , with increasing	
214	integrated charge for RE2 (5.18a) and RE4 (5.18b) detectors. Both	
215	irradiated (blue) and non irradiated (red) chambers are shown. The	
216	integrated charge for non irradiated detectors is recorded during	
217	test beam periods and stays small with respect to the charge accu-	
218	mulated in irradiated chambers.	5-23
219	5.19 Comparison of the efficiency sigmoid before (triangles) and after	
220	(circles) irradiation for RE2 (5.19a) and RE4 (5.19b) detectors.	
221	Both irradiated (blue) and non irradiated (red) chambers are shown. 5-24	
222	5.20 Evolution of the Bakelite resistivity for RE2 (5.20a) and RE4 (5.20b)	
223	detectors. Both irradiated (blue) and non irradiated (red) chambers	
224	are shown.	5-24
225	5.21 Evolution of the noise rate per unit area for the irradiated chamber	
226	RE2-2-BARC-9 only.	5-25
227	A.1 (A.1a) View of the front panel of a V1190A TDC module [10].	
228	(A.1b) View of the front panel of a V1718 Bridge module [11].	
229	(A.1c) View of the front panel of a 6U 6021 VME crate [12]. . . A-4	
230	A.2 Module V1190A <i>Trigger Matching Mode</i> timing diagram [10]. . . A-5	
231	A.3 Structure of the ROOT output file generated by the DAQ. The 5	
232	branches (<code>EventNumber</code> , <code>number_of_hits</code> , <code>Quality_flag</code> , <code>TDC_channel</code>	
233	and <code>TDC_TimeStamp</code>) are visible on the left panel of the ROOT	
234	browser. On the right panel is visible the histogram corresponding	
235	to the variable <code>nHits</code> . In this specific example, there were approxi-	
236	mately 50k events recorded to measure the gamma irradiation rate	
237	on the detectors. Each event is stored as a single entry in the <code>TTree</code> . A-11	
238	A.4 WebDCS DAQ scan page. On this page, shifters need to choose	
239	the type of scan (Rate, Efficiency or Noise Reference scan), the	
240	gamma source configuration at the moment of data taking, the	
241	beam configuration, and the trigger mode. These information will	
242	be stored in the DAQ ROOT output. Are also given the minimal	
243	measurement time and waiting time after ramping up of the detec-	
244	tors is over before starting the data acquisition. Then, the list of	
245	HV points to scan and the number of triggers for each run of the	
246	scan are given in the table underneath.	A-13

List of Tables

248	5.1	Total photon flux ($E\gamma \leq 662$ keV) with statistical error predicted considering a ^{137}Cs activity of 740 GBq at different values of the distance D to the source along the x-axis of irradiation field [6]. . .	5-15
249	5.2	Correction factor c is computed thanks to formulae 5.5 taking as reference $D_0 = 50$ cm and the associated flux F_0^{ABS} for each ab- sorption factor available in table 5.1.	5-16
250	5.3	The data at D_0 in 1997 is taken from [6]. In a second step, using Equations 5.8 and 5.9, the flux at D can be estimated in 1997. Then, taking into account the attenuation of the source activity, the flux at D can be estimated at the time of the tests in GIF in 2014. Finally, assuming a sensitivity of the RPC to γ $s = 2 \cdot 10^{-3}$, an estimation of the hit rate per unit area is obtained.	5-18
251			
252			
253			
254	A.1	Inter-process communication cycles in between the webDCS and the DAQ through file string signals.	A-16
255			
256			
257			
258			
259			

List of Acronyms

262

263

List of Acronyms

264

265

A

266

267

268 AFL

Almost Full Level

269

270

B

271

272

273 BARC

Bhabha Atomic Research Centre

274 BLT

Block Transfer

275 BR

Branching Ratio

276

277

C

278

279

280 CAEN

Costruzioni Apparecchiature Elettroniche Nucleari S.p.A.

281

282 CERN

European Organization for Nuclear Research

283 CFD

Constant Fraction Discriminator

284 CMS

Compact Muon Solenoid

285 CSC

Cathode Strip Chamber

286

287

D

288

289

290 DAQ

Data Acquisition

291 DCS

Detector Control Software

292 DQM

Data Quality Monitoring

293	DT	Drift Tube
294		
295		
296	F	
297		
298	FEE	Front-End Electronics
299	FEB	Front-End Board
300		
301		
302	G	
303		
304	GE-/-	Find a good description
305	GE1/1	Find a good description
306	GE2/1	Find a good description
307	GEANT	GEometry ANd Tracking - a series of software toolkit platforms developed by CERN
308		
309	GEM	Gas Electron Multiplier
310	GIF	Gamma Irradiation Facility
311	GIF++	new Gamma Irradiation Facility
312		
313		
314	H	
315		
316	HL-LHC	High Luminosity LHC
317	HV	High Voltage
318		
319		
320	I	
321		
322	iRPC	improved RPC
323	IRQ	Interrupt Request
324		
325		
326	L	
327		
328	LHC	Large Hadron Collider
329	LS1	First Long Shutdown
330	LS3	Third Long Shutdown

331	LV	Low Voltage
332	LVDS	Low-Voltage Differential Signaling
333		
334		
335	M	
336		
337	MC	Monte Carlo
338	MCNP	Monte Carlo N-Particle
339	ME/-	Find good description
340	ME0	Find good description
341		
342		
343	N	
344		
345	NIM	Nuclear Instrumentation Module logic signals
346		
347		
348	P	
349		
350	PMT	PhotoMultiplier Tube
351		
352		
353	R	
354		
355	RE/-	Find a good description
356	RE2/2	Find a good description
357	RE3/1	Find a good description
358	RE3/2	Find a good description
359	RE4/1	Find a good description
360	RE4/2	Find a good description
361	RE4/3	Find a good description
362	RMS	Root Mean Square
363	ROOT	a framework for data processing born at CERN
364	RPC	Resistive Plate Chamber
365		
366		
367	S	
368		
369	SPS	Super Proton Synchrotron

370

371

372 **T**

373

374 TDC

Time-to-Digital Converter

375

376

377 **W**

378

379 webDCS

Web Detector Control System

381

382

Nederlandse samenvatting –Summary in Dutch–

383 Le resume en Neerlandais (j'aurais peut-etre de apprendre la langue juste pour
384 ca...).

English summary

³⁸⁶ Le meme résume mais en Anglais (on commencera par la hein!).

1

Introduction

387

388

³⁸⁹ **1.1 A story of High Energy Physics**

³⁹⁰ **1.2 Organisation of this study**

2

391

392

Investigating the TeV scale

393 2.1 The Standard Model of Particle Physics

394 2.2 The Large Hadron Collider and the Compact 395 Muon Solenoid

396 2.3 Muon Phase-II Upgrade

397 After the more than two years lasting First Long Shutdown (LS1), the Large
398 Hadron Collider (LHC) delivered its very first Run-II proton-proton collisions
399 early 2015. LS1 gave the opportunity to the LHC and to the its experiments to
400 undergo upgrades. The accelerator is now providing collisions at center-of-mass
401 energy of 13 TeV and bunch crossing rate of 40 MHz, with a peak luminosity ex-
402 ceeding its design value. During the first and upcoming second LHC Long Shut-
403 down, the Compact Muon Solenoid (CMS) detector is also undergoing a number
404 of upgrades to maintain a high system performance [1].

405 From the LHC Phase-2 or High Luminosity LHC (HL-LHC) period onwards,
406 i.e. past the Third Long Shutdown (LS3), the performance degradation due to
407 integrated radiation as well as the average number of inelastic collisions per bunch
408 crossing, or pileup, will rise substantially and become a major challenge for the
409 LHC experiments, like CMS that are forced to address an upgrade program for
410 Phase-II [2]. Simulations of the expected distribution of absorbed dose in the CMS
411 detector under HL-LHC conditions, show in figure 5.14 that detectors placed close

- ⁴¹² to the beamline will have to withstand high irradiation, the radiation dose being of
⁴¹³ the order of a few tens of Gy.

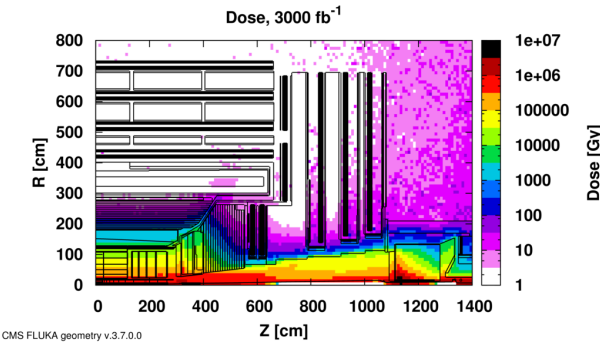


Figure 2.1: Absorbed dose in the CMS cavern after an integrated luminosity of 3000 fb. R is the transverse distance from the beamline and Z is the distance along the beamline from the Interaction Point at Z=0.

⁴¹⁴ The measurement of small production cross-section and/or decay branching
⁴¹⁵ ratio processes, such as the Higgs boson coupling to charge leptons or the $B_s \rightarrow$
⁴¹⁶ $\mu^+ \mu^-$ decay, is of major interest and specific upgrades in the forward regions of
⁴¹⁷ the detector will be required to maximize the physics acceptance on the largest
⁴¹⁸ possible solid angle. To ensure proper trigger performance within the present cov-
⁴¹⁹ erage, the muon system will be completed with new chambers. In figure 2.2 one
⁴²⁰ can see that the existing Cathode Strip Chambers (CSCs) will be completed by Gas
⁴²¹ Electron Multipliers (GEMs) and Resistive Plate Chambers (RPCs) in the pseudo-
⁴²² rapidity region $1.6 < |\eta| < 2.4$ to complete its redundancy as originally scheduled
⁴²³ in the CMS Technical Proposal [3].

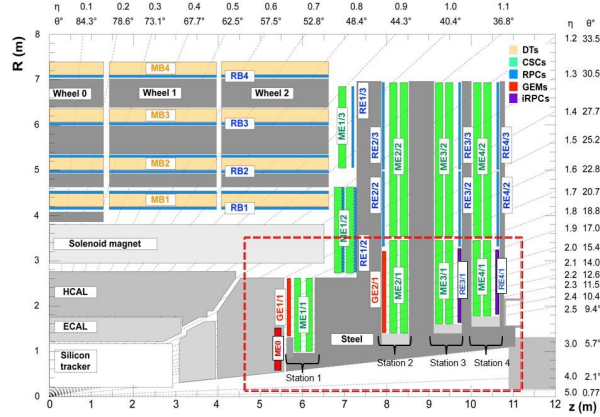


Figure 2.2: A quadrant of the muon system, showing DTs (yellow), RPCs (light blue), and CSCs (green). The locations of new forward muon detectors for Phase-II are contained within the dashed box and indicated in red for GEM stations (ME0, GE1/1, and GE2/1) and dark blue for improved RPC (iRPC) stations (RE3/1 and RE4/1).

424 RPCs are used by the CMS first level trigger for their good timing performances.
 425 Indeed, a very good bunch crossing identification can be obtained with the
 426 present CMS RPC system, given their fast response of the order of 1 ns. In order
 427 to contribute to the precision of muon momentum measurements, muon chambers
 428 should have a spatial resolution less or comparable to the contribution of multiple
 429 scattering [1]. Most of the plausible physics is covered only considering muons
 430 with $p_T < 100$ GeV thus, in order to match CMS requirements, a spatial resolu-
 431 tion of $\mathcal{O}(\text{few mm})$ the proposed new RPC stations, as shown by the simulation in
 432 figure 2.3. According to preliminary designs, RE3/1 and RE4/1 readout pitch will
 433 be comprised between 3 and 6 mm and 5 η -partitions could be considered.

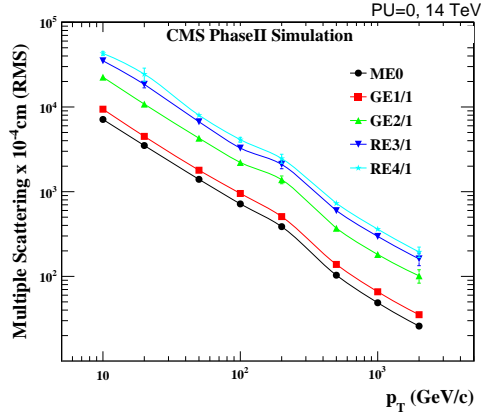


Figure 2.3: RMS of the multiple scattering displacement as a function of muon p_T for the proposed forward muon stations. All of the electromagnetic processes such as bremsstrahlung and magnetic field effect are included in the simulation.

3

434

435

436

Amplification processes in gaseous detectors

437 **3.1 Signal formation**

438 **3.2 Gas transport parameters**

4

439

440

Resistive Plate Chambers

441 4.1 Principle

442 4.2 Rate capability of Resistive Plate Chambers

443 4.3 High time resolution

444 4.4 Resistive Plate Chambers at CMS

445 4.4.1 Overview

446 The Resistive Plate Chambers (RPC) system, located in both barrel and endcap
447 regions, provides a fast, independent muon trigger with a looser p_T threshold over
448 a large portion of the pseudorapidity range ($|\eta| < 1.6$) [\[add reconstruction\]](#).

449

450 During High-Luminosity LHC (HL-LHC) operations the expected conditions
451 in terms of background and pile-up will make the identification and correct P_T as-
452 signment a challenge for the Muon system. The goal of RPC upgrade is to provide
453 additional hits to the Muon system with precise timing. All these informations will
454 be elaborated by the trigger system in a global way enhancing the performance of
455 the trigger in terms of efficiency and rate control. The RPC Upgrade is based
456 on two projects: an improved Link Board System and the extension of the RPC
457 coverage up to $|\eta| = 2.4$. [\[FIXME 2.4 or 2.5?\]](#)

458 The Link Board system, that will be described in section xxx, is responsible to
459 process, synchronize and zero-suppress the signals coming from the RPC front end
460 boards. The Link Board components have been produced between 2006 and 2007
461 and will be subjected to aging and failure in the long term. The upgraded Link
462 Board system will overcome the aging problems described in section xxx and will
463 allow for a more precise timing information to the RPC hits from 25 to 1 ns [ref
464 section xxx].

465 The extension of the RPC system up to $|\eta| = 2.1$ was already planned in the
466 CMS TDR [ref cmstdr] and staged because of budget limitations and expected
467 background rates higher than the rate capability of the present CMS RPCs in that
468 region. An extensive R&D program has been done in order to develop an improved
469 RPC that fulfills the CMS requirements. Two new RPC layers in the innermost ring
470 of stations 3 and 4 will be added with benefits to the neutron-induced background
471 reduction and efficiency improvement for both trigger and offline reconstruction.

472 4.4.2 The present RPC system

473 The RPC system is organized in 4 stations called RB1 to RB4 in the barrel region,
474 and RE1 to RE4 in the endcap region. The innermost barrel stations, RB1 and
475 RB2, are instrumented with 2 layers of RPCs facing the innermost (RB1in and
476 RB2in) and outermost (RB1out and RB2out) sides of the DT chambers. Every
477 chamber is then divided from the read-out point of view into 2 or 3 η partitions
478 called “rolls”. The RPC system consist of 480 barrel chambers and 576 endcap
479 chambers. Details on the geometry are discussed in the paper [ref to geo paper].

480 The CMS RPC chamber is a double-gap, operated in avalanche mode to ensure
481 reliable operation at high rates. Each RPC gap consists of two 2-mm-thick resistive
482 High-Pressure Laminate (HPL) plates separated by a 2-mm-thick gas gap. The
483 outer surface of the HPL plates is coated with a thin conductive graphite layer, and
484 a voltage is applied. The RPCs are operated with a 3-component, non-flammable
485 gas mixture consisting of 95.2% freon ($C_2H_2F_4$, known as R134a), 4.5% isobutane
486 ($i-C_4H_{10}$), and 0.3% sulphur hexafluoride (SF_6) with a relative humidity of 40% -
487 50%. Readout strips are aligned in η between the 2 gas gaps. [\[Add a sentence on
488 FEBs.\]](#)

489 The discriminated signals coming from the Front End boards feed via twisted
490 cables (10 to 20 m long) the Link Board System located in UXC on the balconies
491 around the detector. The Link System consist of the 1376 Link Boards (LBs)
492 and the 216 Control Boards (CBs), placed in 108 Link Boxes. The Link Box
493 is a custom crate (6U high) with 20 slots (for two CBs and eighteen LBs). The
494 Link Box contains custom backplane to which the cables from the chambers are
495 connected, as well as the cables providing the LBs and CBs power supply and the
496 cables for the RPC FEBs control with use of the I2C protocol (trough the CB). The

497 backplane itself contains only connectors (and no any other electronic devices).

498 The Link Board has 96 input channels (one channel corresponds to one RPC
499 strip). The input signals are the ~ 100 ns binary pulses which are synchronous to
500 the RPC hits, but not to the LHC clock (which drives the entire CMS electronics).
501 Thus the first step of the FEB signals processing is synchronization, i.e. assign-
502 ment of the signals to the BXes (25 ns periods). Then the data are compressed with
503 a simple zero-suppressing algorithm (the input channels are grouped into 8 bit par-
504 titions, only the partitions with at least one nonzero bit are selected for each BX).
505 Next, the non-empty partitions are time-multiplexed i.e. if there are more than one
506 such partition in a given BX, they are sent one-by-one in consecutive BXes. The
507 data from 3 neighbouring LBs are concentrated by the middle LB which contains
508 the optical transmitter for sending them to the USC over a fiber at 1.6 Gbps.

509 The Control Boards provide the communication of the control software with
510 the LBs via the FEC/CCU system. The CBs are connected into token rings, each
511 ring consists of 12 CBs of one detector tower and a FEC mezzanine board placed
512 on the CCS board located in the VME crate in the USC. In total, there are 18 rings
513 in the entire Link System. The CBs also perform automatic reloading of the LB's
514 firmware which is needed in order to avoid accumulation of the radiation induced
515 SEUs in the LBs firmware.

516 Both LBs and CB are based on the Xilinx Spartan III FPGAs, the CB addition-
517 ally contains radiation-tolerant (FLASH based) FPGA Actel ProAsicPlus.

518 The High Voltage power system is located in USC, not exposed to radiation and
519 easily accessible for any reparation. A single HV channel powers 2 RPC chambers
520 both in the barrel and endcap regions. The Low Voltage boards are located in UXC
521 on the balconies and provide the voltage to the front end electronics.

522 **4.4.3 Pulse processing of CMS RPCs**

523 Signals induced by cosmic particle in the RPC strips are shaped by standard CMS
524 RPC Front-End Electronics (FEE) following the scheme of Figure 4.1. On a first
525 stage, analogic signals are amplified and then sent to the Constant Fraction Dis-
526 criminator (CFD) described in Figure 4.2. At the end of the chain, 100 ns long
527 pulses are sent in the LVDS output. These output signal are sent on one side to a
528 V1190A Time-to-Digital Converter (TDC) module from CAEN and on the other
529 to an OR module to count the number of detected signals. Trigger and hit coïnci-
530 dences are monitored using scalers. The TDC is used to store the data into ROOT
531 files. These files are thus analysed to understand the detectors performance.

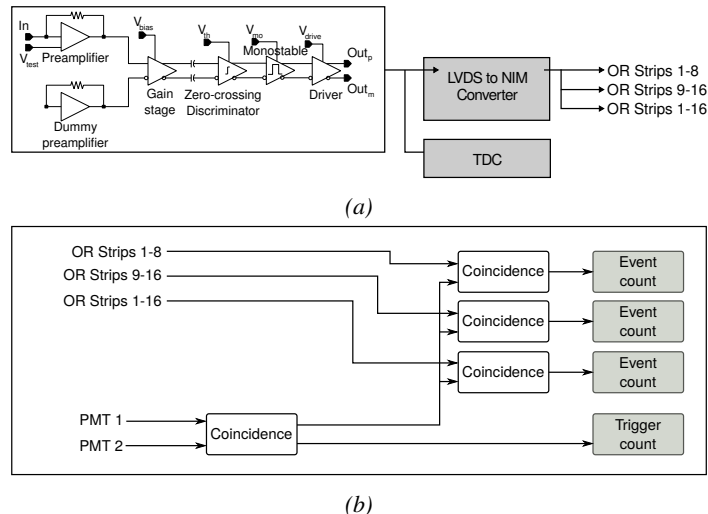


Figure 4.1: Signals from the RPC strips are shaped by the FEE described on Figure 4.1a. Output LVDS signals are then read-out by a TDC module connected to a computer or converted into NIM and sent to scalers. Figure 4.1b describes how these converted signals are put in coincidence with the trigger.

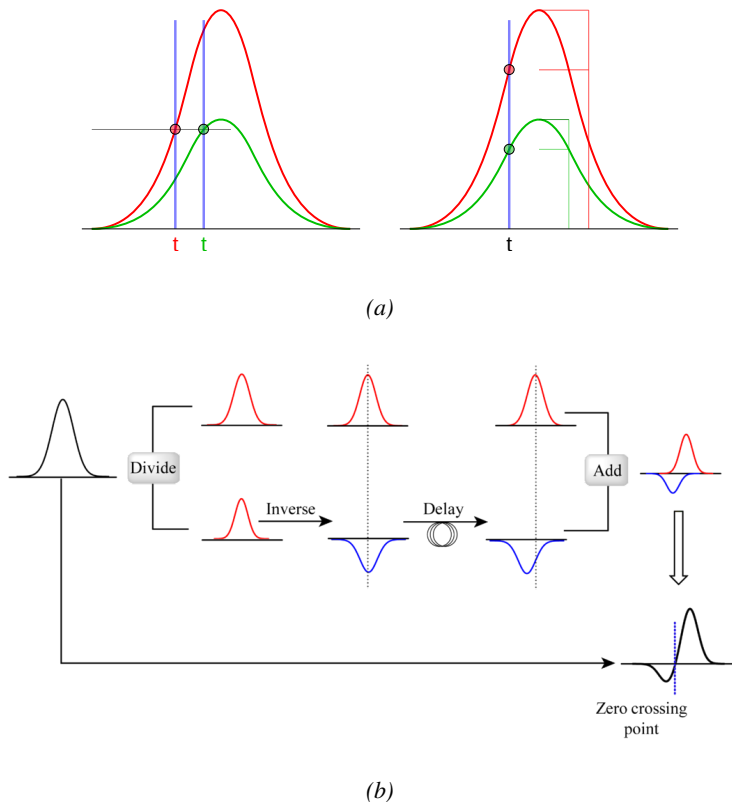


Figure 4.2: Description of the principle of a CFD. A comparison of threshold triggering (left) and constant fraction triggering (right) is shown in Figure 4.2a. Constant fraction triggering is obtained thanks to zero-crossing technique as explained in Figure 4.2b. The signal arriving at the input of the CFD is split into three components. A first one is delayed and connected to the inverting input of a first comparator. A second component is connected to the noninverting input of this first comparator. A third component is connected to the noninverting input of another comparator along with a threshold value connected to the inverting input. Finally, the output of both comparators is fed through an AND gate.

5

532

533 Longevity studies and Consolidation of 534 the present CMS RPC subsystem

535 5.1 Testing detectors under extreme conditions

536 The upgrade from LHC to HL-LHC will increase the peak luminosity from 10^{34}
537 $\text{cm}^{-2} \text{s}^{-1}$ to reach $5 \times 10^{34} \text{ cm}^{-2} \text{s}^{-1}$, increasing in the same way the total ex-
538 pected background to which the RPC system will be subjected to. Composed of
539 low energy gammas and neutrons from p - p collisions, low momentum primary
540 and secondary muons, puch-through hadrons from calorimeters, and particles pro-
541 duced in the interaction of the beams with collimators, the background will mostly
542 affect the regions of CMS that are the closest to the beam line, i.e. the RPC detec-
543 tors located in the endcaps. [To update.]

544

545 The 2016 data allowed to study the values of the background rate in all RPC
546 system. In Figure 5.1, the distribution of the chamber background hit rate per unit
547 area is shown at a luminosity of $5 \times 10^{34} \text{ cm}^{-2} \cdot \text{s}^{-1}$ linearly extrapolating from
548 data collected in 2016 [ref mentioning the linear dependency of rate vs lumi]. The
549 maximum rate per unit area at HL-LHC conditions is expected to be of the or-
550 der of 600 Hz/cm^2 (including a safety factor 3). Nevertheless, Fluka simulations
551 have conducted in order to understand the background at HL-LHC conditions. The
552 comparison to the data has shown, in Figure 5.2, a discrepancy of a factor 2 even
553 though the order of magnitude is consistent. [Understand mismatch.]

554

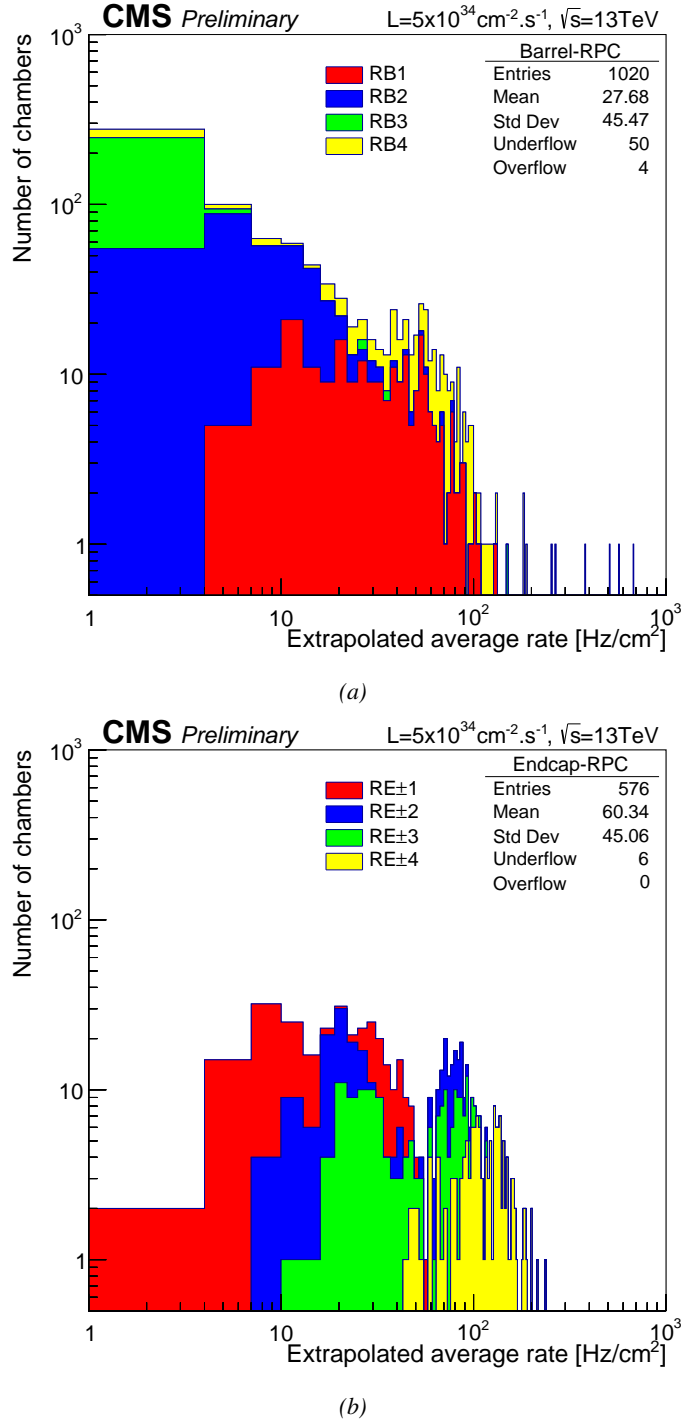


Figure 5.1: (5.1a) Extrapolation from 2016 data of single hit rate per unit area in the barrel region. (5.1b) Extrapolation from 2016 data of single hit rate per unit area in the endcap region.

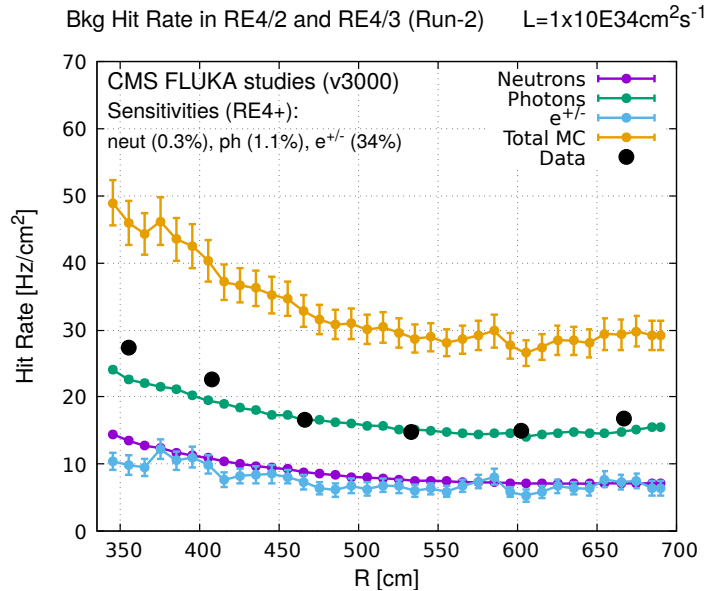


Figure 5.2: Background Fluka simulation compared to 2016 Data at $L = 10^{34} \text{ cm}^{-2} \cdot \text{s}^{-1}$ in the fourth endcap disk region. A mismatch in between simulation and data can be observed. [\[To be understood.\]](#)

555 In the past, extensive long-term tests were carried out at several gamma and
 556 neutron facilities certifying the detector performance. Both full size and small
 557 prototype RPCs have been irradiated with photons up to an integrated charge of
 558 $\sim 0.05 \text{ C}/\text{cm}^2$ and $\sim 0.4 \text{ C}/\text{cm}^2$, respectively [4, 5]. During Run-I, the RPC sys-
 559 tem provided stable operation and excellent performance and did not show any
 560 aging effects for integrated charge of the order of $0.01 \text{ C}/\text{cm}^2$. Projections on cur-
 561 rents from 2016 Data, has allowed to determine that the total integrated charge, by
 562 the end of HL-LHC, would be of the order of $1 \text{ C}/\text{cm}^2$ (including a safety factor
 563 3). [\[Corresponding figure needed.\]](#)

564

565 5.1.1 The Gamma Irradiation Facilities

566 5.1.1.1 GIF

567 Located in the SPS West Area at the downstream end of the X5 test beam, the
 568 Gamma Irradiation Facility (GIF) was a test area in which particle detectors were
 569 exposed to a particle beam in presence of an adjustable gamma background [6].
 570 Its goal was to reproduce background conditions these detectors would suffer in
 571 their operating environment at LHC. GIF layout is shown in Figure 5.3. Gamma

572 photons are produced by a strong ^{137}Cs source installed in the upstream part of the
 573 zone inside a lead container. The source container includes a collimator, designed
 574 to irradiate a $6 \times 6 \text{ m}^2$ area at 5 m maximum to the source. A thin lens-shaped lead
 575 filter helps providing with a uniform outgoing flux in a vertical plane, orthogonal
 576 to the beam direction. The principal collimator hole provides a pyramidal aperture
 577 of $74^\circ \times 74^\circ$ solid angle and provides a photon flux in a pyramidal volume along
 578 the beam axis. The photon rate is controled by further lead filters allowing the
 579 maximum rate to be limited and to vary within a range of four orders of magni-
 580 tude. Particle detectors under test are then placed within the pyramidal volume
 581 in front of the source, perpendicularly to the beam line in order to profit from the
 582 homogeneous photon flux. Adjusting the background flux of photons can then be
 583 done by using the filters and choosing the position of the detectors with respect to
 584 the source.

585

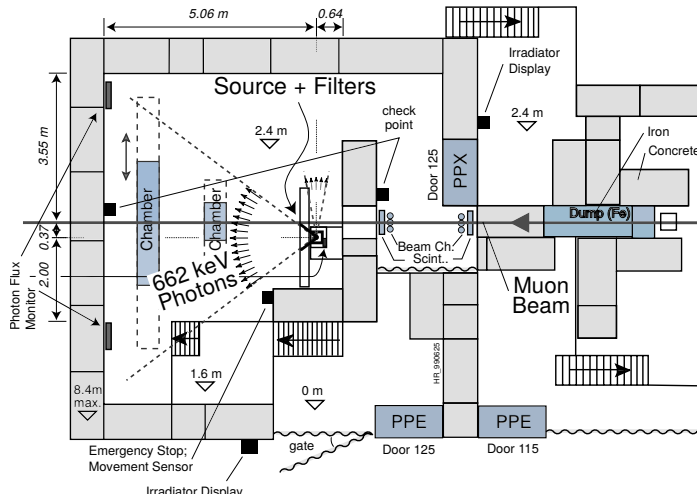


Figure 5.3: Layout of the test beam zone called X5c GIF at CERN. Photons from the radioactive source produce a sustained high rate of random hits over the whole area. The zone is surrounded by 8 m high and 80 cm thick concrete walls. Access is possible through three entry points. Two access doors for personnel and one large gate for material. A crane allows installation of heavy equipment in the area.

586 As described on Figure 5.4, the ^{137}Cs source emits a 662 keV photon in 85%
 587 of the decays. An activity of 740 GBq was measured on the 5th March 1997. To
 588 estimate the strength of the flux in 2014, it is necessary to consider the nuclear
 589 decay through time assiciated to the Cesium source whose half-life is well known
 590 ($t_{1/2} = (30.05 \pm 0.08) \text{ y}$). The GIF tests where done in between the 20th and the
 591 31st of August 2014, i.e. at a time $t = (17.47 \pm 0.02) \text{ y}$ resulting in an attenuation

592 of the activity from 740 GBq in 1997 to 494 GBq in 2014.

593

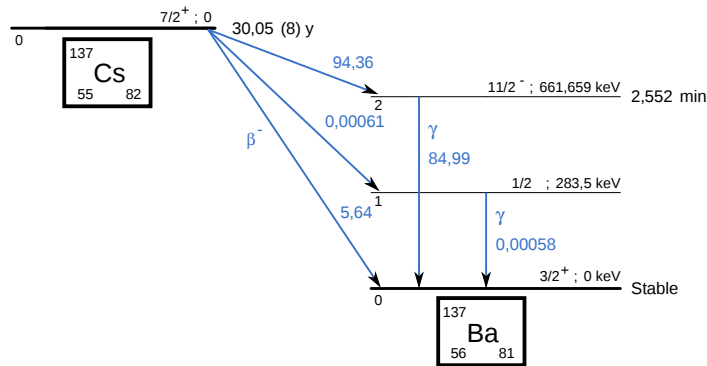


Figure 5.4: ^{137}Cs decays by β^- emission to the ground state of ^{137}Ba ($BR = 5.64\%$) and via the 662 keV isomeric level of ^{137}Ba ($BR = 94.36\%$) whose half-life is 2.55 min.

594 5.1.1.2 GIF++

595 The new Gamma Irradiation Facility (GIF++), located in the SPS North Area at
 596 the downstream end of the H4 test beam, has replaced its predecessor during LS1
 597 and has been operational since spring 2015 [7]. Like GIF, GIF++ features a ^{137}Cs
 598 source of 662 keV gamma photons, their fluence being controlled with a set of
 599 filters of various attenuation factors. The source provides two separated large irra-
 600 diation areas for testing several full-size muon detectors with continuous homo-
 601 geneous irradiation, as presented in Figure 5.5.

602

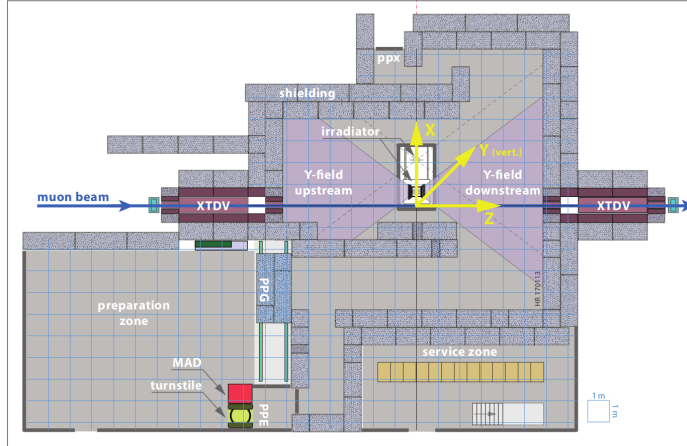


Figure 5.5: Floor plan of the GIF++ facility. When the facility downstream of the GIF++ takes electron beam, a beam pipe is installed along the beam line (z -axis). The irradiator can be displaced laterally (its center moves from $x = 0.65$ m to 2.15 m), to increase the distance to the beam pipe.

603 The source activity was measured to be about 13.5 TBq in March 2016. The
 604 photon flux being far greater than HL-LHC expectations, GIF++ provides an ex-
 605 cellent facility for accelerated aging tests of muon detectors.
 606

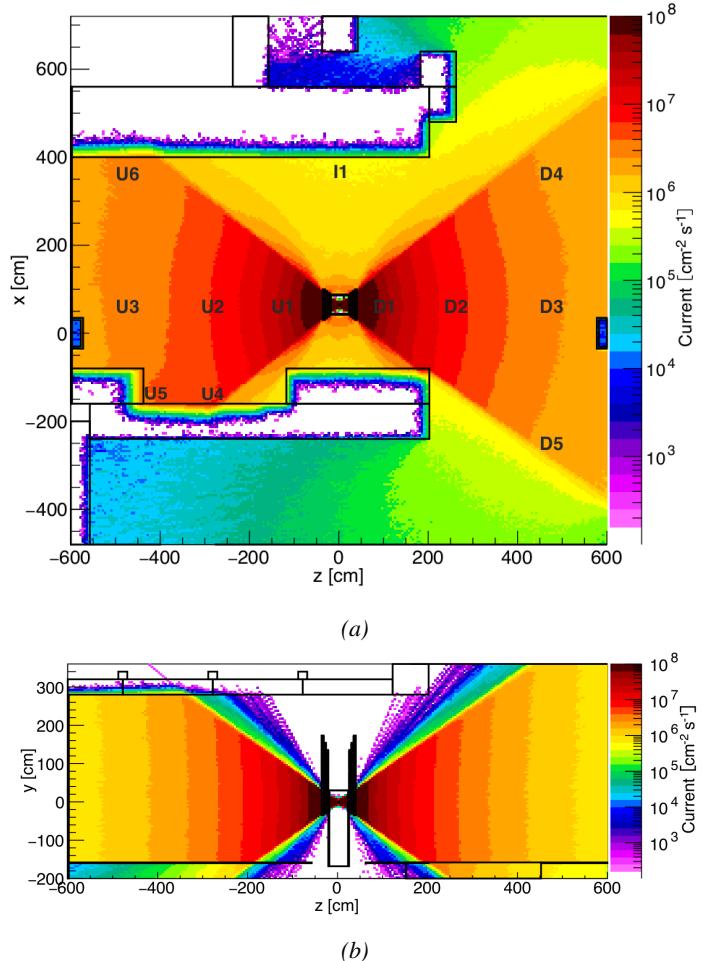


Figure 5.6: Simulated unattenuated current of photons in the xz plane (Figure 5.6a) and yz plane (Figure 5.6b) through the source at $x = 0.65$ m and $y = 0$ m. With angular correction filters, the current of 662 keV photons is made uniform in xy planes.

607 The source is situated in the muon beam line with the muon beam being avail-
 608 able a few times a year. The H4 beam, composed of muons with a momentum of
 609 about 150 GeV/c, passes through the GIF++ zone and is used to study the per-
 610 formance of the detectors. Its flux is of 104 particles/s/cm² focused in an area
 611 similar to 10×10 cm². Therefore, with properly adjusted filters, one can imitate
 612 the HL-LHC background and study the performance of muon detectors with their
 613 trigger/readout electronics in HL-LHC environment.
 614

615 5.2 Preliminary tests at GIF

616 5.2.1 Resistive Plate Chamber test setup

617 During summer 2014, preliminary tests have been conducted in the GIF area on
 618 a newly produced RE4/2 chamber labelled RE-4-2-BARC-161. This chamber has
 619 been placed into a trolley covered with a tent. The position of the RPC inside the
 620 tent and of the tent related to the source is described in Figure 5.7. To test this
 621 CMS RPC, three different absorber settings were used. First of all, measurements
 622 were done with fully opened source. Then, to complete this preliminary study,
 623 the gamma flux has been attenuated from a factor 2 and a factor 5. The expected
 624 gamma flux at the level of our detector will be discussed in subsection 5.2.4.

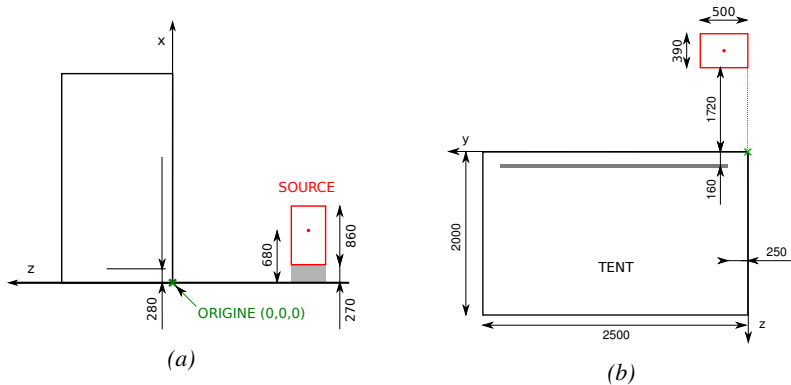


Figure 5.7: Description of the RPC setup. Dimensions are given in mm. A tent containing RPCs is placed at 1720 mm from the source container. The source is situated in the center of the container. RE-4-2-BARC-161 chamber is 160 mm inside the tent. This way, the distance between the source and the chambers plan is 2060 mm. Figure 5.7a provides a side view of the setup in the xz plane while Figure 5.7b shows a top view in the yz plane.



Figure 5.8: RE-4-2-BARC-161 chamber is inside the tent as described in Figure 5.7. In the top right, the two scintillators used as trigger can be seen. This trigger system has an inclination of 10° relative to horizontal and is placed above half-partition B2 of the RPCs. PMT electronics are shielded thanks to lead blocks placed in order to protect them without stopping photons from going through the scintillators and the chamber.

625 At the time of the tests, the beam not being operational anymore, a trigger
626 composed of 2 plastic scintillators has been placed in front of the setup with an
627 inclination of 10 deg with respect to the detector plane in order to look at cosmic
628 muons. Using this particular trigger layout, shown on Figure 5.8, leads to a cosmic
629 muon hit distribution into the chamber similar to the one in Figure 5.9. Measured
630 without gamma irradiation, two peaks can be seen on the profil of partition B, cen-
631 tered on strips 52 and 59. Section 5.2.3 will help us understand that these two peaks
632 are due respectively to forward and backward coming cosmic particles where for-
633 ward coming particles are first detected by the scintillators and then the RPC while
634 the backward coming muons are first detected in the RPC.

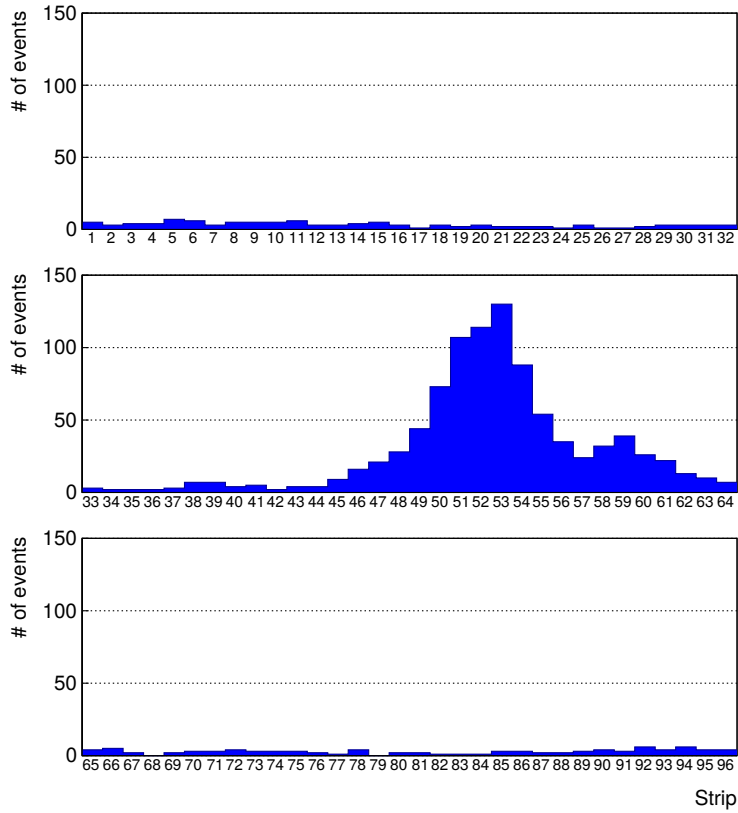


Figure 5.9: Hit distributions over all 3 partitions of RE-4-2-BARC-161 chamber is showed on these plots. Top, middle and bottom figures respectively correspond to partitions A, B, and C. These plots show that some events still occur in other half-partitions than B2, which corresponds to strips 49 to 64, in front of which the trigger is placed, contributing to the inefficiency of detection of cosmic muons. In the case of partitions A and C, the very low amount of data can be interpreted as noise. On the other hand, it is clear that a little portion of muons reach the half-partition B1, corresponding to strips 33 to 48.

635 5.2.2 Data Acquisition

636 5.2.3 Geometrical acceptance of the setup layout to cosmic muons

637 In order to profit from a constant gamma irradiation, the detectors inside of the GIF
 638 bunker need to be placed in a plane orthogonal to the beam line. The muon beam
 639 that used to be available was meant to test the performance of detectors under test.
 640 This beam not being active anymore, another solution to test detector performance
 641 had to be used. Thus, it has been decided to use cosmic muons detected through

642 a telescope composed of two scintillators. Lead blocks were used as shielding to
 643 protect the photomultipliers from gammas as can be seen from Figure 5.8.

644 An inclination has been given to the cosmic telescope to maximize the muon
 645 flux. A good compromise had to be found between good enough muon flux and
 646 narrow enough hit distribution to be sure to contain all the events into only one half
 647 partitions as required from the limited available readout hardware. Nevertheless,
 648 a consequence of the misplaced trigger, that can be seen as a loss of events in
 649 half-partition B1 in Figure 5.9, is an inefficiency. Nevertheless, the inefficiency
 650 of approximately 20 % highlighted in Figure 5.10 by comparing the performance
 651 of chamber BARC-161 in 904 and at GIF without irradiation seems too important
 652 to be explained only by the geometrical acceptance of the setup itself. Simulations
 653 have been conducted to show how the setup brings inefficiency.

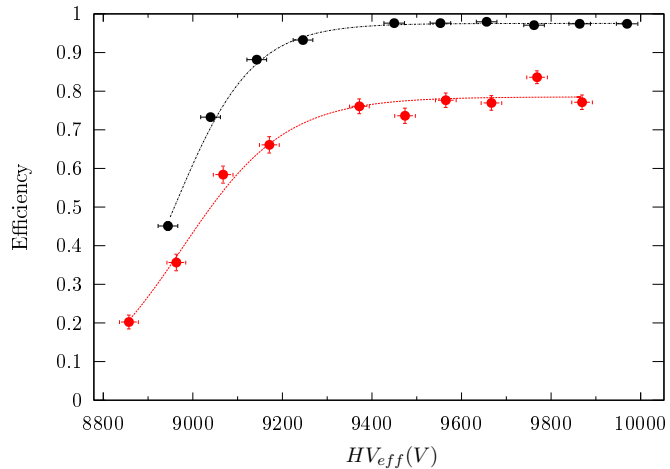


Figure 5.10: Results are derived from data taken on half-partition B2 only. On the 18th of June 2014, data has been taken on chamber RE-2-BARC-161 at building 904 (Prevessin Site) with cosmic muons providing us a reference efficiency plateau of $(97.54 \pm 0.15)\%$ represented by a black curve. A similar measurement has been done at GIF on the 21st of July with the same chamber giving a plateau of $(78.52 \pm 0.94)\%$ represented by a red curve.

654 5.2.3.1 Description of the simulation layout

655 The layout of GIF setup has been reproduced and incorporated into a Monte Carlo
 656 (MC) simulation to study the influence of the disposition of the telescope on the
 657 final distribution measured by the RPC. A 3D view of the simulated layout is given
 658 into Figure 5.11. Muons are generated randomly in a horizontal plane located at a
 659 height corresponding to the lowest point of the PMTs. This way, the needed size
 660 of the plane in order to simulate events happening at very big azimuthal angles (i.e.

661 $\theta \approx \pi$) can be kept relatively small. The muon flux is designed to follow the usual
 662 $\cos^2\theta$ distribution for cosmic particle. The goal of the simulation is to look at
 663 muons that pass through the muon telescope composed of the two scintillators and
 664 define their distribution onto the RPC plane. During the reconstruction, the RPC
 665 plane is then divided into its strips and each muon track is assigned to a strip.

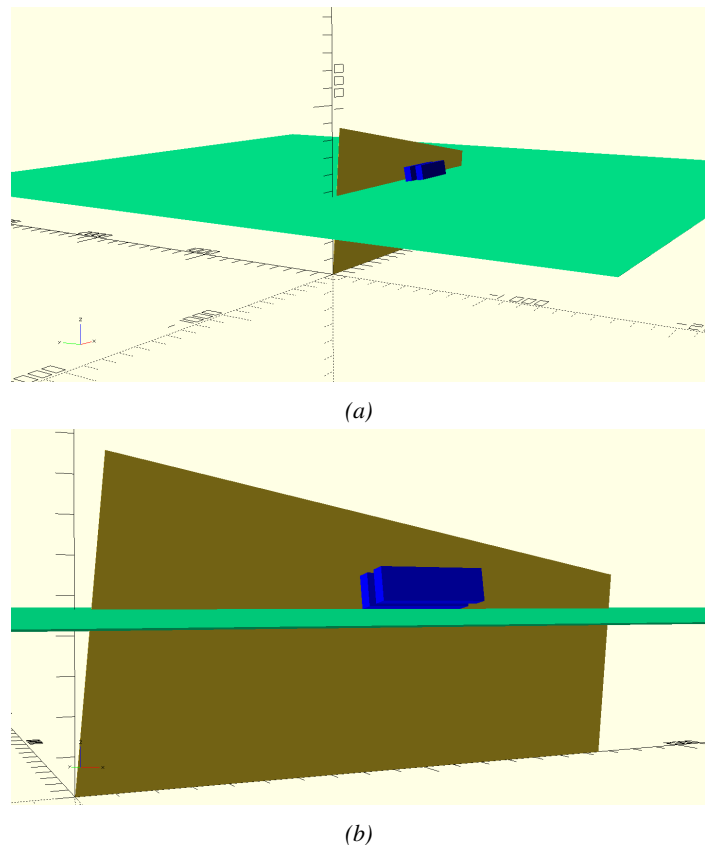


Figure 5.11: Representation of the layout used for the simulations of the test setup. The RPC is represented as a yellow trapezoid while the two scintillators as blue cuboids looking at the sky. A green plane corresponds to the muon generation plane within the simulation. Figure 5.7a shows a global view of the simulated setup. Figure 5.7b shows a zoomed view that allows to see the 2 scintillators as well as the full RPC plane.

666 In order to further refine the quality of the simulation and understand deeper
 667 the results the dependance of the distribution has been studied for a range of tele-
 668 scope inclinations. Moreover, the threshold applied on the PMT signals has been
 669 included into the simulation in the form of a cut. In the approximation of uni-
 670 form scintillators, it has been considered that the threshold can be understood as

671 the minimum distance particles need to travel through the scintillating material to
672 give a strong enough signal. Particles that travel a distance smaller than the set
673 "threshold" are thus not detected by the telescope and cannot trigger the data tak-
674 ing. Finally, the FEE threshold also has been considered in a similar way. The
675 mean momentum of horizontal cosmic rays is higher than those of vertical ones
676 but the stopping power of matter for momenta ranging from 1 GeV to 1 TeV stays
677 comparable. It is then possible to assume that the mean number of primary e^-/ion
678 pairs per unit length will stay similar and thus, depending on the applied discrimi-
679 nator threshold, muons with the shortest path through the gas volume will deposit
680 less charge and induce a smaller signal on the pick-up strips that could eventu-
681 ally not be detected. These two thresholds also restrain the overall geometrical
682 acceptance of the system.

683 **5.2.3.2 Simulation procedure**

684 The simulation software has been designed using C++ and the output data is saved
685 into ROOT histograms. Simulations start for a threshold T_{scint} varying in a range
686 from 0 to 45 mm in steps of 5 mm, where $T_{scint} = 0 \text{ mm}$ corresponds to the case
687 where there isn't any threshold apply on the input signal while $T_{scint} = 45 \text{ mm}$,
688 which is the scintillator thickness, is the case where muons cannot arrive orthogo-
689 nally onto the scintillator surface. For a given T_{scint} , a set of RPC thresholds are
690 considered. The RPC threshold, T_{RPC} varies from 2 mm, the thickness of the gas
691 volume, to 3 mm in steps of 0.25 mm. For each $(T_{scint}; T_{RPC})$ pair, $N_\mu = 10^8$
692 muons are randomly generated inside the muon plane described in the previous
693 paragraph with an azimuthal angle θ chosen to follow a $\cos^2\theta$ distribution.

694 Planes are associated to each surface of the scintillators. Knowing muon posi-
695 tion into the muon plane and its direction allows us, by assuming that muons travel
696 in a straight line, to compute the intersection of the muon track with these planes.
697 Applying conditions to the limits of the surfaces of the scintillator faces then gives
698 us an answer to whether or not the muon passed through the scintillators. In the
699 case the muon has indeed passed through the telescope, the path through each scin-
700 tillator is computed and muons whose path was shorter than T_{scint} are rejected and
701 are thus considered as having not interacted with the setup.

702 On the contrary, if the muon is labeled as good, its position within the RPC
703 plane is computed and the corresponding strip, determined by geometrical tests
704 in the case the distance through the gas volume was enough not to be rejected
705 because of T_{RPC} , gets a hit and several histograms are filled in order to keep
706 track of the generation point on the muon plane, the intersection points of the
707 reconstructed muons within the telescope, or on the RPC plane, the path traveled
708 through each individual scintillator or the gas volume, as well as other histograms.
709 Moreover, muons fill different histograms whether they are forward or backward
710 coming muons. They are discriminated according to their direction components.

711 When a muon is generated, an (x, y, z) position is assigned into the muon plane as
 712 well as a $(\theta; \phi)$ pair that gives us the direction it's coming from. This way, muons
 713 satisfying the condition $0 \leq \phi < \pi$ are designated as backward coming muons
 714 while muons satisfying $\pi \leq \phi < 2\pi$ as forward coming muons.

715 This simulation is then repeated for different telescope inclinations ranging in
 716 between 4 and 20° and varying in steps of 2° . Due to this inclination and to the
 717 vertical position of the detector under test, the muon distribution reconstructed in
 718 the detector plane is asymmetrical. The choice has been made to chose a skew
 719 distribution formula to fit the data built as the multiplication of gaussian and sig-
 720 moidal curves together. A typical gaussian formula is given as 5.1 and has three
 721 free parameters as A_g , its amplitude, \bar{x} , its mean value and σ , its root mean square.
 722 Sigmoidal curves as given by formula 5.2 are functions converging to 0 and A_s as
 723 x diverges. The inflexion point is given as x_i and λ is proportional to the slope at
 724 $x = x_i$. In the limit where $\lambda \rightarrow \infty$, the sigmoid becomes a step function.

$$g(x) = A_g e^{\frac{-(x-\bar{x})^2}{2\sigma^2}} \quad (5.1)$$

$$s(x) = \frac{A_s}{1 + e^{-\lambda(x-x_i)}} \quad (5.2)$$

725 Finally, a possible representation of a skew distribution is given by formula 5.3
 726 and is the product of 5.1 and 5.2. Naturally, here $A_{sk} = A_g \times A_s$ and represents
 727 the theoretical maximum in the limit where the skew tends to a gaussian function.

$$sk(x) = g(x) \times s(x) = A_{sk} \frac{e^{\frac{-(x-\bar{x})^2}{2\sigma^2}}}{1 + e^{-\lambda(x-x_i)}} \quad (5.3)$$

728 5.2.3.3 Results

729 Influence of T_{scint} on the muon distribution

730 Influence of T_{RPC} on the muon distribution

731 Influence of the telescope inclination on the muon distribution

732 Comparison to data taken at GIF without irradiation

733 **5.2.4 Photon flux at GIF**

734 **5.2.4.1 Expectations from simulations**

735 In order to understand and evaluate the γ flux in the GIF area, simulations had been
 736 conducted in 1999 and published by S. Agosteo et al [6]. Table 5.1 presented in
 737 this article gives us the γ flux for different distances D to the source. This sim-
 738 ulation was done using GEANT and a Monte Carlo N-Particle (MCNP) transport
 739 code, and the flux F is given in number of γ per unit area and unit time along with
 740 the estimated error from these packages expressed in %.

Nominal ABS	Photon flux F [$s^{-1}cm^{-2}$]			
	at $D = 50$ cm	at $D = 155$ cm	at $D = 300$ cm	at $D = 400$ cm
1	$0.12 \cdot 10^8 \pm 0.2\%$	$0.14 \cdot 10^7 \pm 0.5\%$	$0.45 \cdot 10^6 \pm 0.5\%$	$0.28 \cdot 10^6 \pm 0.5\%$
2	$0.68 \cdot 10^7 \pm 0.3\%$	$0.80 \cdot 10^6 \pm 0.8\%$	$0.25 \cdot 10^6 \pm 0.8\%$	$0.16 \cdot 10^6 \pm 0.6\%$
5	$0.31 \cdot 10^7 \pm 0.4\%$	$0.36 \cdot 10^6 \pm 1.2\%$	$0.11 \cdot 10^6 \pm 1.2\%$	$0.70 \cdot 10^5 \pm 0.9\%$

Table 5.1: Total photon flux ($E\gamma \leq 662$ keV) with statistical error predicted considering a ^{137}Cs activity of 740 GBq at different values of the distance D to the source along the x-axis of irradiation field [6].

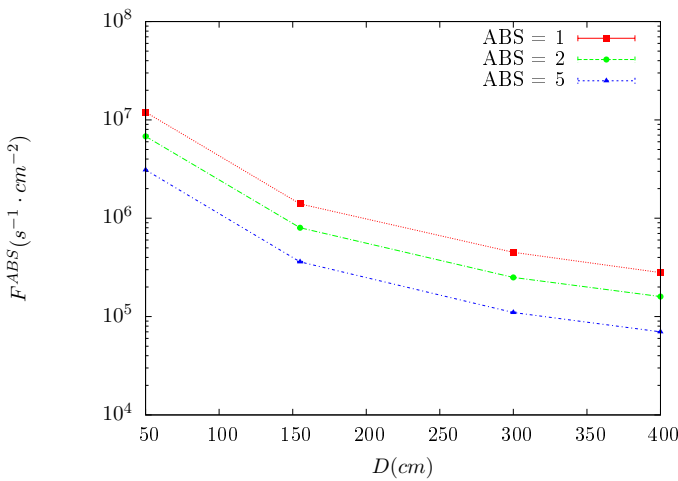


Figure 5.12: γ flux $F(D)$ is plot using values from table 5.1. As expected, the plot shows similar attenuation behaviours with increasing distance for each absorption factors.

741 The simulation doesn't directly provides us with an estimated flux at the level
 742 of our RPC. First of all, it is needed to extract the value of the flux from the
 743 available data contained in the original paper and then to estimate the flux in 2014
 744 at the time the experimentation took place. Figure 5.12 that contains the data from

745 Table 5.1. In the case of a pointlike source emitting isotropic and homogeneous
 746 gamma radiations, the gamma flux F at a distance D to the source with respect
 747 to a reference point situated at D_0 where a known flux F_0 is measured will be
 748 expressed like in Equation 5.4, assuming that the flux decreases as $1/D^2$, where c
 749 is a fitting factor.

$$F^{ABS} = F_0^{ABS} \times \left(\frac{cD_0}{D} \right)^2 \quad (5.4)$$

750 By rewriting Equation 5.4, it comes that :

$$c = \frac{D}{D_0} \sqrt{\frac{F^{ABS}}{F_0^{ABS}}} \quad (5.5)$$

$$\Delta c = \frac{c}{2} \left(\frac{\Delta F^{ABS}}{F^{ABS}} + \frac{\Delta F_0^{ABS}}{F_0^{ABS}} \right) \quad (5.6)$$

751 Finally, using Equation 5.5 and the data in Table 5.1 with $D_0 = 50$ cm as
 752 reference point, we can build Table 5.2. It is interesting to note that c for each
 753 value of D doesn't depend on the absorption factor.

Nominal ABS	Correction factor c		
	at $D = 155$ cm	at $D = 300$ cm	at $D = 400$ cm
1	$1.059 \pm 0.70\%$	$1.162 \pm 0.70\%$	$1.222 \pm 0.70\%$
2	$1.063 \pm 1.10\%$	$1.150 \pm 1.10\%$	$1.227 \pm 0.90\%$
5	$1.056 \pm 1.60\%$	$1.130 \pm 1.60\%$	$1.202 \pm 1.30\%$

Table 5.2: Correction factor c is computed thanks to formulae 5.5 taking as reference $D_0 = 50$ cm and the associated flux F_0^{ABS} for each absorption factor available in table 5.1.

754 For the range of D/D_0 values available, it is possible to use a simple linear
 755 fit to get the evolution of c . The linear fit will then use only 2 free parameters, a
 756 and b , as written in Equation 5.7. This gives us the results showed in Figure 5.13.
 757 Figure 5.13b confirms that using only a linear fit to extract c is enough as the
 758 evolution of the rate that can be obtained superimposes well on the simulation
 759 points.

$$c \left(\frac{D}{D_0} \right) = a \frac{D}{D_0} + b \quad (5.7)$$

$$F^{ABS} = F_0^{ABS} \left(a + \frac{bD_0}{D} \right)^2 \quad (5.8)$$

$$\Delta F^{ABS} = F^{ABS} \left[\frac{\Delta F_0^{ABS}}{F_0^{ABS}} + 2 \frac{\Delta a + \Delta b \frac{D_0}{D}}{a + \frac{bD_0}{D}} \right] \quad (5.9)$$

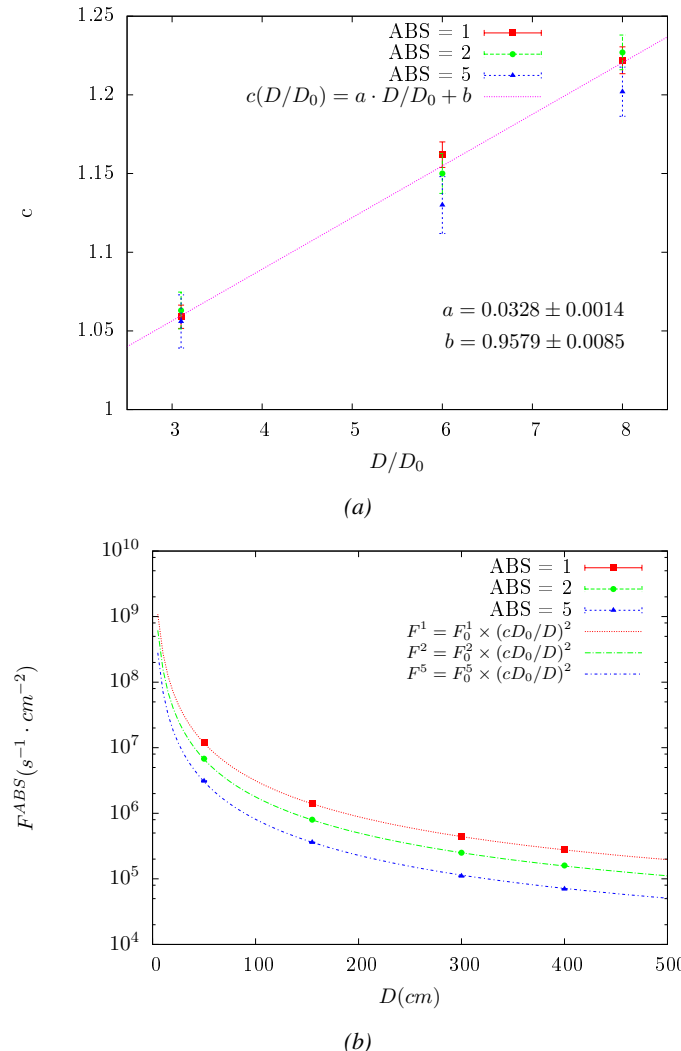


Figure 5.13: Figure 5.13a shows the linear approximation fit done via formulae 5.7 on data from table 5.2. Figure 5.13b shows a comparison of this model with the simulated flux using a and b given in figure 5.13a in formulae 5.4 and the reference value $D_0 = 50\text{cm}$ and the associated flux for each absorption factor F_0^{ABS} from table 5.1

In the case of the 2014 GIF tests, the RPC plane is located at a distance $D = 206\text{ cm}$ to the source. Moreover, to estimate the strength of the flux in 2014, it is necessary to consider the nuclear decay through time associated to the Cesium source whose half-life is well known ($t_{1/2} = (30.05 \pm 0.08)\text{ y}$). The very first source activity measurement has been done on the 5th of March 1997 while the

765 GIF tests were done between the 20th and the 31st of August 2014, i.e. at a
 766 time $t = (17.47 \pm 0.02)$ y resulting in an attenuation of the activity from 740 GBq
 767 in 1997 to 494 GBq in 2014. All the needed information to extrapolate the flux
 768 through our detector in 2014 has now been assembled, leading to the Table 5.3. It
 769 is interesting to note that for a common RPC sensitivity to γ of $2 \cdot 10^{-3}$, the order
 770 of magnitude of the estimated hit rate per unit area is of the order of the kHz for
 771 the fully opened source. Moreover, taking profit of the two working absorbers, it
 772 will be possible to scan background rates at 0 Hz, ~ 300 Hz as well as ~ 600 Hz.
 773 Without source, a good estimate of the intrinsic performance will be available.
 774 Then at 300 Hz, the goal will be to show that the detectors fulfill the performance
 775 certification of CMS RPCs. Then a first idea of the performance of the detectors at
 776 higher background will be provided with absorption factors 2 (~ 600 Hz) and 1 (no
 777 absorption). *[Here I will also put a reference to the plot showing the estimated
 778 background rate at the level of RE3/I in the case of HL-LHC but this one being
 779 in another chapter, I will do it later.]*

Nominal ABS	Photon flux F [$s^{-1}cm^{-2}$]			Hit rate/unit area [$Hz cm^{-2}$] at $D^{2014} = 206$ cm
	at $D_0^{1997} = 50$ cm	at $D_0^{1997} = 206$ cm	at $D^{2014} = 206$ cm	
1	$0.12 \cdot 10^8 \pm 0.2\%$	$0.84 \cdot 10^6 \pm 0.3\%$	$0.56 \cdot 10^6 \pm 0.3\%$	1129 ± 32
2	$0.68 \cdot 10^7 \pm 0.3\%$	$0.48 \cdot 10^6 \pm 0.3\%$	$0.32 \cdot 10^6 \pm 0.3\%$	640 ± 19
5	$0.31 \cdot 10^7 \pm 0.4\%$	$0.22 \cdot 10^6 \pm 0.3\%$	$0.15 \cdot 10^6 \pm 0.3\%$	292 ± 9

Table 5.3: The data at D_0 in 1997 is taken from [6]. In a second step, using Equations 5.8 and 5.9, the flux at D can be estimated in 1997. Then, taking into account the attenuation of the source activity, the flux at D can be estimated at the time of the tests in GIF in 2014. Finally, assuming a sensitivity of the RPC to γ $s = 2 \cdot 10^{-3}$, an estimation of the hit rate per unit area is obtained.

780 **5.2.4.2 Dose measurements**

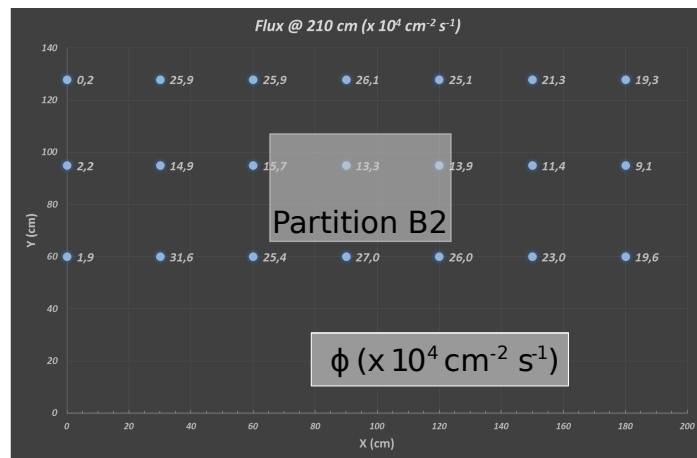


Figure 5.14: Dose measurements has been done in a plane corresponding to the tents front side. This plan is 1900 mm away from the source. As explained in the first chapter, a lens-shaped lead filter provides a uniform photon flux in the vertical plan orthogonal to the beam direction. If the second line of measured fluxes is not taken into account because of lower values due to experimental equipments in the way between the source and the tent, the uniformity of the flux is well showed by the results.

⁷⁸¹ **5.2.5 Results and discussions**

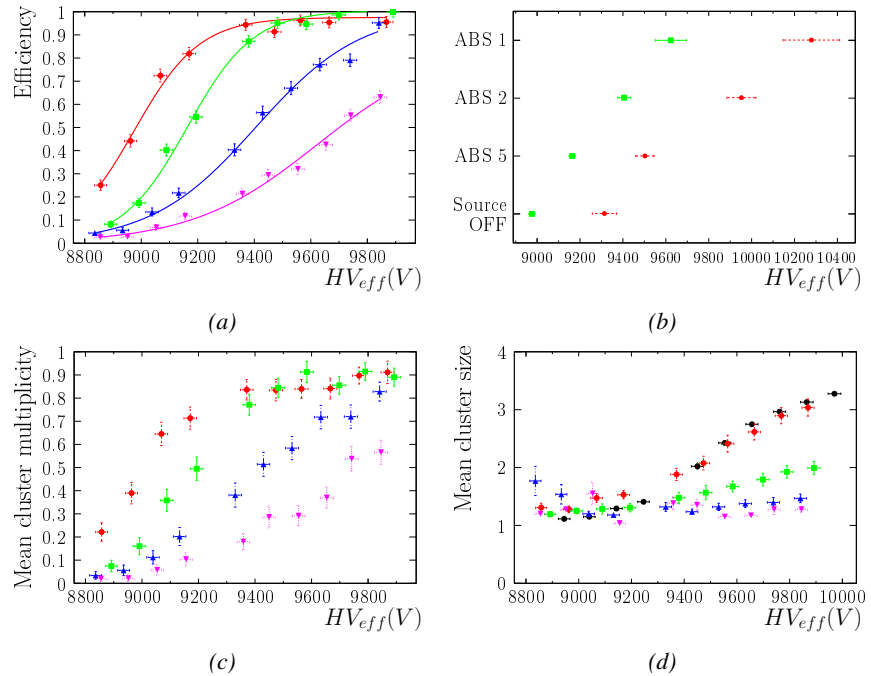


Figure 5.15

5.3 Longevity tests at GIF++

782 Longevity studies imply a monitoring of the performance of the detectors probed
783 using a high intensity muon beam in a irradiated environment by periodically mea-
784 suring their rate capability, the dark current running through them and the bulk
785 resistivity of the Bakelite composing their electrodes. GIF++, with its very intense
786 ^{137}Cs source, provides the perfect environment to perform such kind of tests. As-
787 suming a maximum acceleration factor of 3, it is expected to accumulate the equiv-
788 alent charge in 1.7 years.

789 As the maximum background is found in the endcap, the choice naturally was
790 made to focus the GIF++ longevity studies on endcap chambers. Most of the RPC
791 system was installed in 2007. Nevertheless, the large chambers in the fourth end-
792 cap (RE4/2 and RE4/3) have been installed during LS1 in 2014. The Bakelite of
793 these two different productions having different properties, four spare chambers
794 of the present system were selected, two RE2,3/2 spares and two RE4/2 spares.
795 Having two chambers of each type allows to always keep one of them non irradia-
796 ted as reference, the performance evolution of the irradiated chamber being then
797 compared through time to the performance of the non irradiated one.

798 The performance of the detectors under different level of irradiation is measured
799 periodically during dedicated test beam periods using the H4 muon beam. In be-
800 tween these test beam periods, the two RE2,3/2 and RE4/2 chambers selected for
801 this study are irradiated by the ^{137}Cs source in order to accumulate charge and
802 the gamma background is monitored, as well as the currents. The two remaining
803 chambers are kept non-irradiated as reference detectors. Due to the limited gas
804 flow in GIF++, the RE4 chamber remained non-irradiated until end of November
805 2016 where a new mass flow controller has been installed allowing for bigger vol-
806 umes of gas to flow in the system.

807 Figures 5.16 and 5.17 give us for different test beam periods, and thus for in-
808 creasing integrated charge through time, a comparison of the maximum efficiency,
809 obtained using a sigmoid-like function, and of the working point of both irradiated
810 and non irradiated chambers [8]. No aging is yet to see from this data, the shifts in
811 γ rate per unit area in between irradiated and non irradiated detectors and RE2 and
812 RE4 types being easily explained by a difference of sensitivity due to the various
813 Bakelite resistivities of the HPL electrodes used for the electrode production.

814 Collecting performance data at each test beam period allows us to extrapolate the
815 maximum efficiency for a background hit rate of 300 Hz/cm^2 corresponding to
816 the expected HL-LHC conditions. Aging effects could emerge from a loss of ef-
817 ficiency with increasing integrated charge over time, thus Figure 5.18 helps us
818 understand such degradation of the performance of irradiated detectors in compar-
819 ison with non irradiated ones. The final answer for an eventual loss of efficiency is
820 given in Figure 5.19 by comparing for both irradiated and non irradiated detectors

the efficiency sigmoids before and after the longevity study. Moreover, to complete the performance information, the Bakelite resistivity is regularly measured thanks to Ag scans (Figure 5.20) and the noise rate is monitored weekly during irradiation periods (Figure 5.21). At the end of 2016, no signs of aging were observed and further investigation is needed to get closer to the final integrated charge requirements proposed for the longevity study of the present CMS RPC sub-system.

828

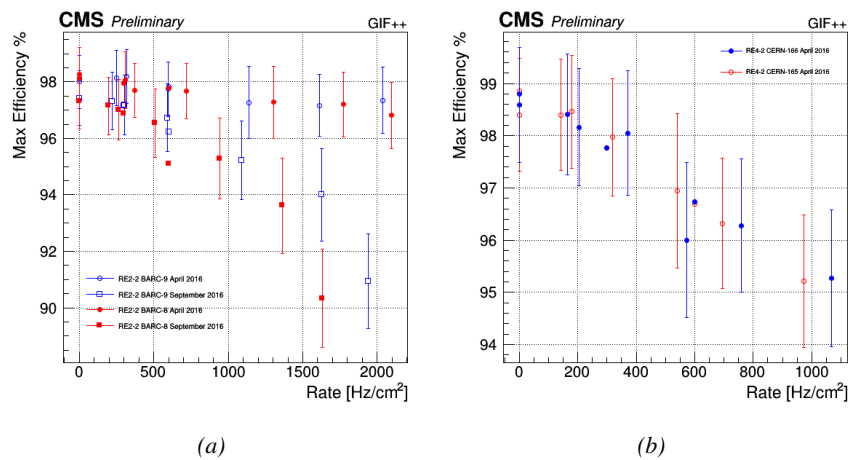


Figure 5.16: Evolution of the maximum efficiency for RE2 (5.16a) and RE4 (5.16b) chambers with increasing extrapolated γ rate per unit area at working point. Both irradiated (blue) and non-irradiated (red) chambers are shown.

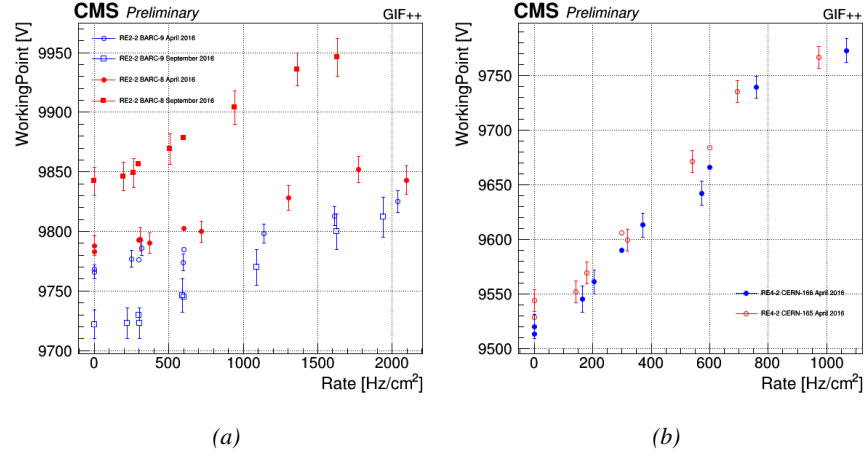


Figure 5.17: Evolution of the working point for RE2 (5.17a) and RE4 (5.17b) with increasing extrapolated γ rate per unit area at working point. Both irradiated (blue) and non irradiated (red) chambers are shown.

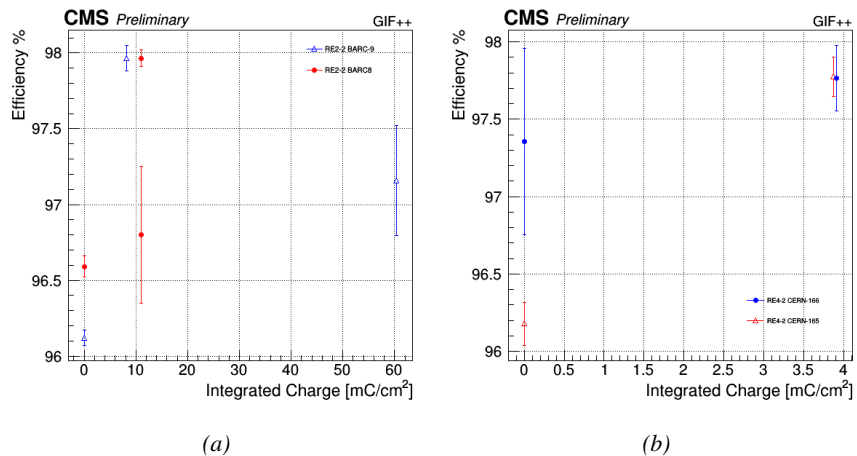


Figure 5.18: Evolution of the maximum efficiency at HL-LHC conditions, i.e. a background hit rate per unit area of 300 Hz/cm², with increasing integrated charge for RE2 (5.18a) and RE4 (5.18b) detectors. Both irradiated (blue) and non irradiated (red) chambers are shown. The integrated charge for non irradiated detectors is recorded during test beam periods and stays small with respect to the charge accumulated in irradiated chambers.

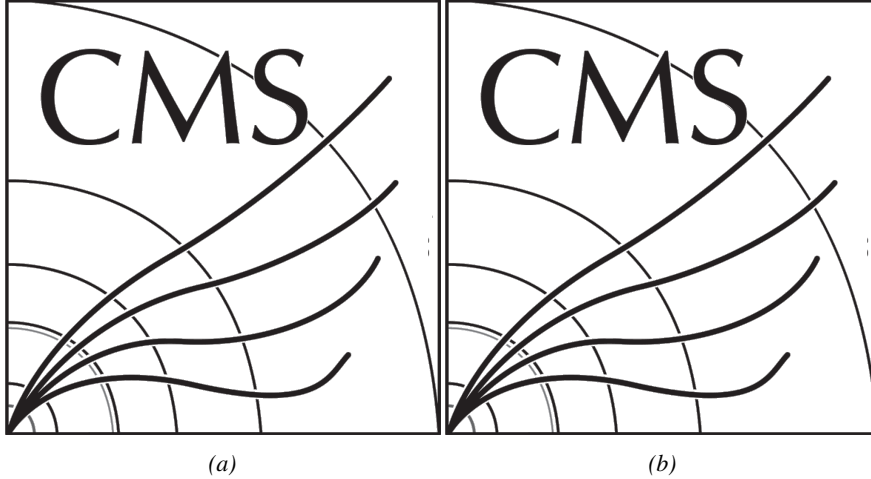


Figure 5.19: Comparison of the efficiency sigmoid before (triangles) and after (circles) irradiation for RE2 (5.19a) and RE4 (5.19b) detectors. Both irradiated (blue) and non irradiated (red) chambers are shown.

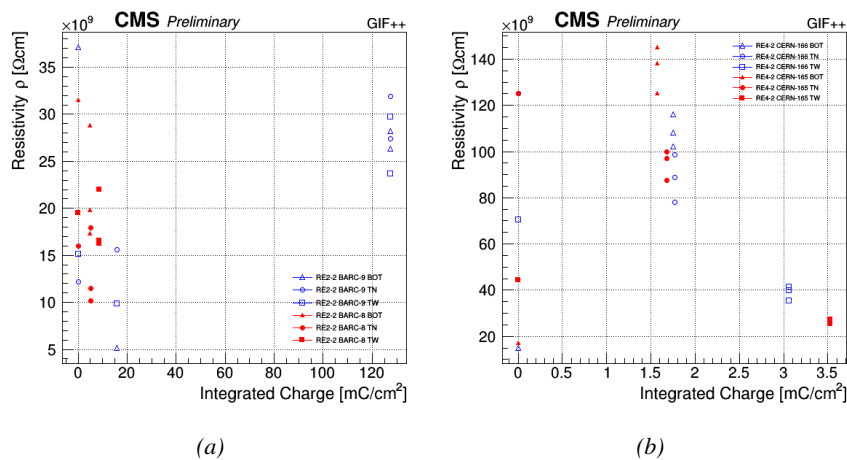


Figure 5.20: Evolution of the Bakelite resistivity for RE2 (5.20a) and RE4 (5.20b) detectors. Both irradiated (blue) and non irradiated (red) chambers are shown.

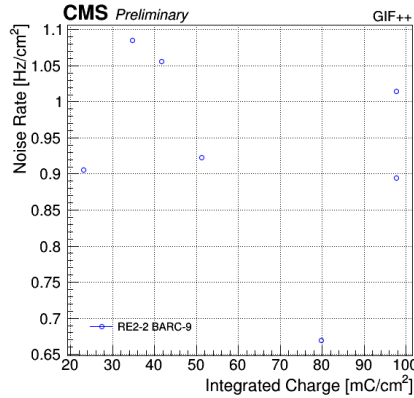


Figure 5.21: Evolution of the noise rate per unit area for the irradiated chamber RE2-2-BARC-9 only.

5.3.1 Description of the Data Acquisition

For the longevity studies, four spare chambers of the present system are used. Two spare RPCs of the RE2,3 stations as well as two spare RPCs from the new RE4 stations have been mounted in a Trolley. Six RE4 gaps are also placed in the trolley. The trolley is placed inside the GIF++ in the upstream region of the bunker, taking the cesium source as a reference. The trolley is oriented for the detection surface of the chambers to be orthogonal to the beam line. The system can be moved along the orthogonal plane in order to have the beam in all η -partitions. For the aging the trolley is moved outside the beam line and is placed in a distance of 5.2 m to the source, which irradiates the bunker using an attenuation filter of 2.2 which corresponds to a fluence of 10^7 gamma/cm².

During GIF++ operation, the data collected can be divided into different categories as several parameters are monitored in addition to the usual RPC performance data. On one hand, to know the performance of a chamber, it is need to measure its efficiency and to know the background conditions in which it is operated. To do this, the hit signals from the chamber are recorded and stored in a ROOT file via a Data Acquisition (DAQ) software. On the other hand, it is also very important to monitor parameters such as environmental pressure and temperature, gas temperature and humidity, RPC HV, LV, and currents, or even source and beam status. This is done through the GIF++ web Detector Control Software (DCS) that stores this information in a database.

Two different types of tests are conducted on RPCs via the DAQ. Indeed, the performance of the detectors is measured periodically during dedicated test beam periods using the H4 muon beam. In between these test beam periods, when the beam is not available, the chambers are irradiated by the ^{137}Cs in order to accu-

854 mulate deposited charge and the gamma background is measured.

855 RPCs under test are connected through LVDS cables to V1190A Time-to-
 856 Digital Converter (TDC) modules manufactured by CAEN. These modules, lo-
 857 cated in the rack area outside of the bunker, get the logic signals sent by the cham-
 858 bers and save them into their buffers. Due to the limited size of the buffers, the
 859 collected data is regularly erased and replaced. A trigger signal is needed for the
 860 TDC modules to send the useful data to the DAQ computer via a V1718 CAEN
 861 USB communication module.

862 In the case of performance test, the trigger signal used for data acquisition is
 863 generated by the coincidence of three scintillators. A first one is placed upstream
 864 outside of the bunker, a second one is placed downstream outside of the bunker,
 865 while a third one is placed in front of the trolley, close by the chambers. Every time
 866 a trigger is sent to the TDCs, i.e. every time a muon is detected, knowing the time
 867 delay in between the trigger and the RPC signals, signals located in the right time
 868 window are extracted from the buffers and saved for later analysis. Signals are
 869 taken in a time window of 400 ns centered on the muon peak (here we could show
 870 a time spectrum). On the other hand, in the case of background rate measurement,
 871 the trigger signal needs to be "random" not to measure muons but to look at gamma
 872 background. A trigger pulse is continuously generated at a rate of 300 Hz using a
 873 dual timer. To integrate an as great as possible time, all signals contained within
 874 a time window of 10us prior to the random trigger signal are extracted form the
 875 buffers and saved for further analysis (here another time spectrum to illustrate
 876 could be useful, maybe even place both spectrum together as a single Figure).

877 The signals sent to the TDCs correspond to hit collections in the RPCs. When a
 878 particle hits a RPC, it induce a signal in the pickup strips of the RPC readout. If this
 879 signal is higher than the detection threshold, a LVDS signal is sent to the TDCs.
 880 The data is then organised into 4 branches keeping track of the event number, the
 881 hit multiplicity for the whole setup, and the time and channel profile of the hits in
 882 the TDCs.

883 **5.3.2 RPC current, environmental and operation parameter mon- 884 itoring**

885 In order to take into account the variation of pressure and temperature between
 886 different data taking periods the applied voltage is corrected following the rela-
 887 tionship :

$$888 \quad HV_{eff} = HV_{app} \times \left(0.2 + 0.8 \cdot \frac{P_0}{P} \times \frac{T}{T_0} \right) \quad (5.10)$$

where T_0 (=293 K) and P_0 (=990 mbar) are the reference values.

889 5.3.3 Measurement procedure

- 890 Insert a short description of the online tools (DAQ, DCS, DQM).
- 891 Insert a short description of the offline tools : tracking and efficiency algorithm.
- 892 Identify long term aging effects we are monitoring the rates per strip.

893 5.3.4 Longevity studies results

6

894

895

Investigation on high rate RPCs

896 **6.1 Rate limitations and ageing of RPCs**

897 **6.1.1 Low resistivity electrodes**

898 **6.1.2 Low noise front-end electronics**

899 **6.2 Construction of prototypes**

900 **6.3 Results and discussions**

7

901

902

Conclusions and outlooks

903 **7.1 Conclusions**

904 **7.2 Outlooks**

References

905

- 906 [1] CERN. Geneva. LHC Experiments Committee. *The CMS muon project :
907 Technical Design Report*. Tech. rep. CERN-LHCC-97-032. CMS Collabora-
908 ration, 1997.
- 909 [2] CERN. Geneva. LHC Experiments Committee. *Technical Proposal for the
910 Phase-II Upgrade of the CMS Detector*. Tech. rep. CERN-LHCC-2015-010.
911 CMS Collaboration, 2015.
- 912 [3] CERN. Geneva. LHC Experiments Committee. *CMS, the Compact Muon
913 Solenoid : technical proposal*. Tech. rep. CERN-LHCC-94-38. CMS Col-
914 laboration, 1994.
- 915 [4] M. Abbrescia et al. “Study of long-term performance of CMS RPC under
916 irradiation at the CERN GIF”. In: *NIMA* 533 (2004), pp. 102–106.
- 917 [5] H.C. Kim et al. “Quantitative aging study with intense irradiation tests for
918 the CMS forward RPCs”. In: *NIMA* 602 (2009), pp. 771–774.
- 919 [6] S. Agosteo et al. “A facility for the test of large-area muon chambers at high
920 rates”. In: *NIMA* 452 (2000), pp. 94–104.
- 921 [7] PoS, ed. *CERN GIF ++ : A new irradiation facility to test large-area par-
922 ticle detectors for the high-luminosity LHC program*. Vol. TIPP2014. 2014,
923 pp. 102–109.
- 924 [8] M. Abbrescia et al. “Cosmic ray tests of double-gap resistive plate chambers
925 for the CMS experiment”. In: *NIMA* 550 (2005), pp. 116–126.
- 926 [9] A. Fagot. *GIF++ DAQ v4.0*. 2017. URL: https://github.com/afagot/GIF_DAQ.
- 928 [10] CAEN. *Mod. V1190-VX1190 A/B, 128/64 Ch Multihit TDC*. 14th ed. 2016.
- 929 [11] CAEN. *Mod. V1718 VME USB Bridge*. 9th ed. 2009.
- 930 [12] W-Ie-Ne-R. *VME 6021-23 VXI*. 5th ed. 2016.
- 931 [13] Wikipedia. *INI file*. 2017. URL: https://github.com/afagot/GIF_DAQ.
- 932

A

933

934 A data acquisition software for CAEN 935 VME TDCs

936 Certifying detectors in the perspective of HL-LHC required to develop tools for the
937 GIF++ experiment. Among them was the C++ Data Acquisition (DAQ) software
938 that allows to make the communications in between the computer and the TDC
939 modules in order to retrieve the RPC data [9]. In this appendix, details about the
940 software, as of how the software was written, how it functions and how it can be
941 exported to another similar setup.

942 **A.1 GIF++ DAQ file tree**

943 GIF++ DAQ source code is fully available on github at https://github.com/afagot/GIF_DAQ. The software requires 3 non-optional dependencies:

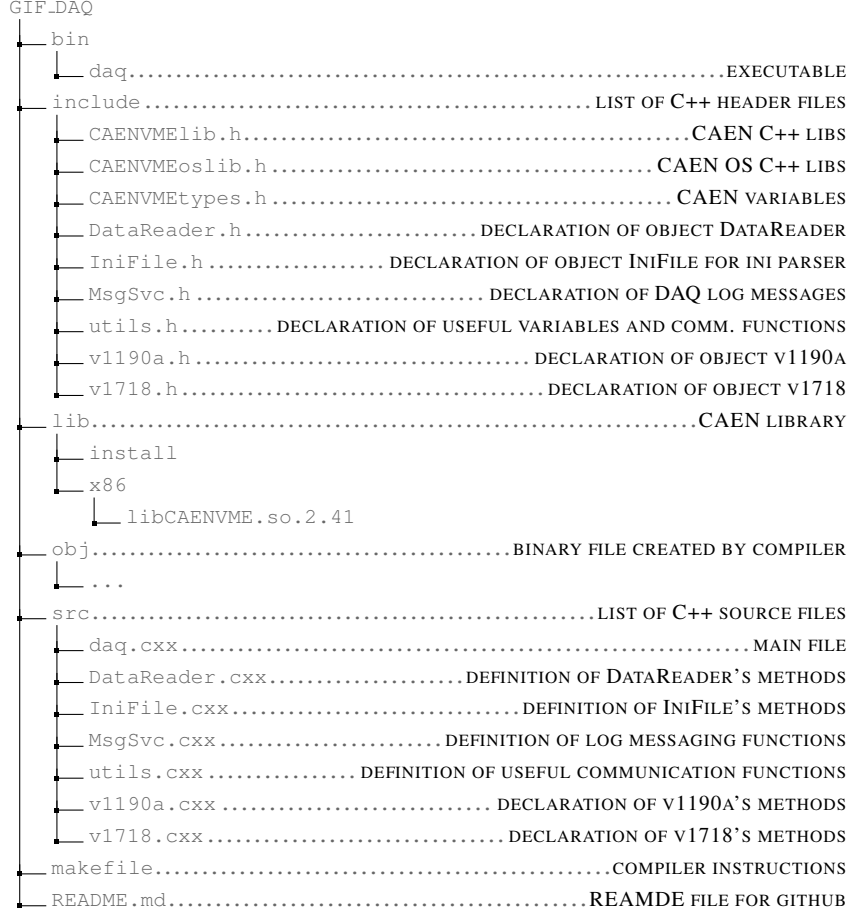
- 945 • CAEN USB Driver to mount the VME hardware
- 946 • CAEN VME Library to communicate with the VME hardware
- 947 • ROOT to organize the collected data into a TTree

948 The CAEN VME library will not be packaged by distributions and will need
949 to be installed manually. To compile the GIF++ DAQ project via a terminal, from
950 the DAQ folder use the command :

951 `make`

952 The source code tree is provided below along with comments to give an overview
 953 of the files' content. The different objects created for this project (v1718, v1190a,
 954 IniFile & DataReader) will be described in details in the following sections.

955



956 **A.2 Usage of the DAQ**

957 GIF++ DAQ as used in GIF++ is not a standalone software. Indeed, the system
 958 being more complexe, the DAQ only is a sub-layer of the software architecture
 959 developped to control and monitor the RPCs that are placed into the bunker for
 960 performance study in an irradiated environment. The top layer of GIF++ is a Web
 961 Detector Control System (webDCS) application. The DAQ is only called by the
 962 webDCS when data needs to be acquired. The webDCS operates the DAQ through
 963 command line. To start the DAQ, the webDCS calls:

```

964      bin/daq /path/to/the/log/file/in/the/output/data/folder
965      where /path/to/the/log/file/in/the/output/data/folder is the only ar-
966      gument required. This log file is important for the webDCS as this file contains
967      all the content of the communication of the webDCS and the different systems
968      monitored by the webDCS. Its content is constantly displayed during data taking
969      for the users to be able to follow the operations. The communication messages are
970      normally sent to the webDCS log file via the functions declared in file MsgSvc.h,
971      typically MSG_INFO(string message).
972
973      Nonetheless, it is possible to make the DAQ a standalone program that could be
974      adapted to any VME setup using V1190A and V1718 modules by creating a GUI
975      for the software or by printing the log messages that are normally printed in the
976      webDCS through the log file, into the terminal.
977

```

978 A.3 Description of the readout setup

```

979 The CMS RPC setup at GIF++ counts 5 V1190A Time-to-Digital Converter (TDC)
980 manufactured by CAEN [10]. V1190A are VME units accepting 128 independent
981 Multi-Hit/Multi-Event TDC channels whose signals are treated by 4 100 ps high
982 performance TDC chips developped by CERN / ECP-MIC Division. The com-
983 munication between the computer and the TDCs to transfer data is done via a
984 V1718 VME master module also manufactured by CAEN and operated from a
985 USB port [11]. These VME modules are all hosted into a 6U VME 6021 pow-
986 ered crate manufactured by W-Ie-Ne-R than can accomodate up to 21 VME bus
987 cards [12]. These 3 components of the DAQ setup are shown in Figure A.1.
988

```

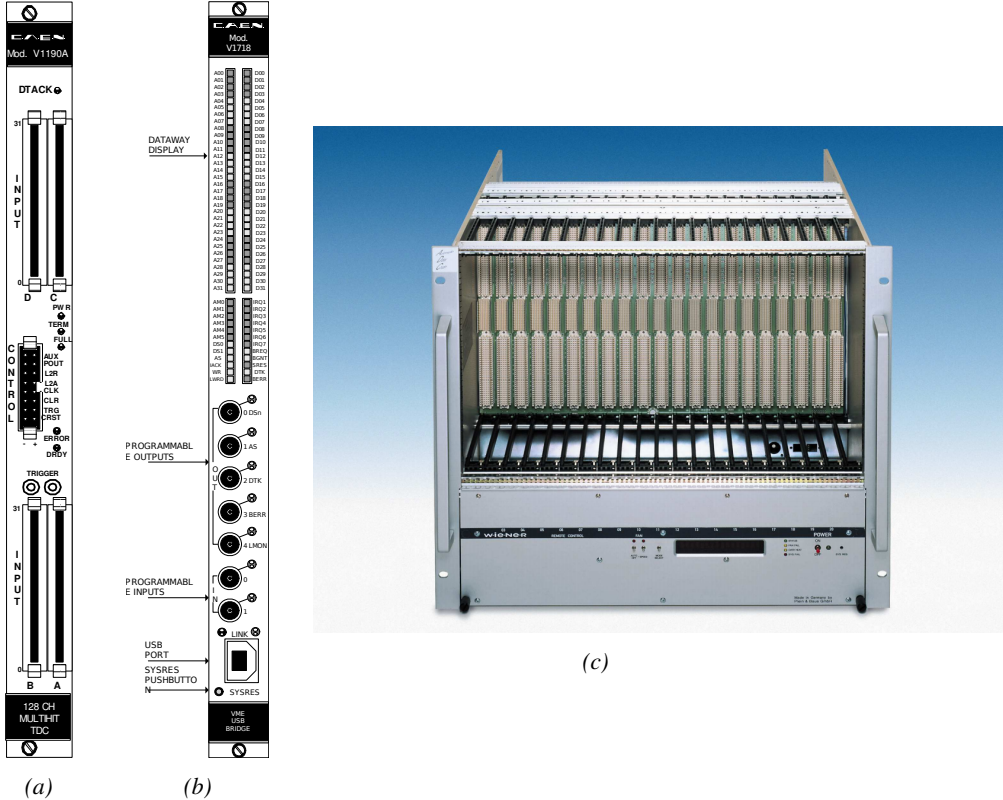


Figure A.1: (A.1a) View of the front panel of a V1190A TDC module [10]. (A.1b) View of the front panel of a V1718 Bridge module [11]. (A.1c) View of the front panel of a 6U 6021 VME crate [12].

989 A.4 Data read-out

990 To efficiently perform a data readout algorithm, C++ objects to handle the VME
 991 modules (TDCs and VME bridge) have been created along with objects to store
 992 data and read the configuration file that comes as an input of the DAQ software.
 993

994 A.4.1 V1190A TDCs

995 The DAQ used at GIF takes profit of the *Trigger Matching Mode* offered by V1190A
 996 modules. This setting is enabled through the method `v1190a::SetTrigMatching`
 997 (`int ntcdcs`) where `ntcdcs` is the total number of TDCs in the setup this setting
 998 needs to be enabled for (Source Code A.1). A trigger matching is performed in
 999 between a trigger time tag, a trigger signal sent into the TRIGGER input of the

1000 TDC visible on Figure A.1a, and the channel time measurements, signals recorded
 1001 from the detectors under test in our case. Control over this data acquisition mode,
 1002 explained through Figure A.2, is offered via 4 programmable parameters:

- 1003 • **match window:** the matching between a trigger and a hit is done within a
 1004 programmable time window. This is set via the method
`1005 void v1190a::SetTrigWindowWidth(UINT windowWidth, INT ntdcs)`
- 1006 • **window offset:** temporal distance between the trigger tag and the start of
 1007 the trigger matching window. This is set via the method
`1008 void v1190a::SetTrigWindowWidth(UINT windowWidth, INT ntdcs)`
- 1009 • **extra search margin:** an extended time window is used to ensure that all
 1010 matching hits are found. This is set via the method
`1011 void v1190a::SetTrigSearchMargin(UINT searchMargin, INT ntdcs)`
- 1012 • **reject margin:** older hits are automatically rejected to prevent buffer over-
 1013 flows and to speed up the search time. This is set via the method
`1014 void v1190a::SetTrigRejectionMargin(UINT rejectMargin, INT ntdcs)`

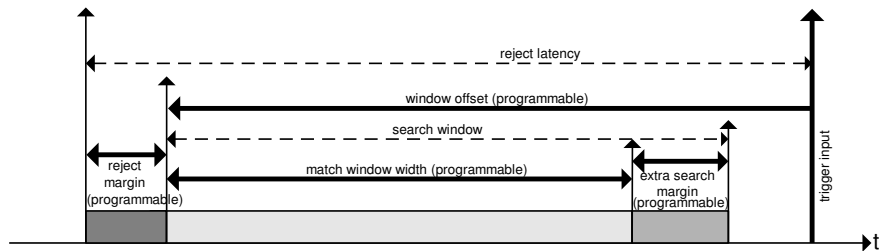


Figure A.2: Module V1190A Trigger Matching Mode timing diagram [10].

1015 Each of these 4 parameters are given in number of clocks, 1 clock being 25 ns
 1016 long. It is easy to understand at this level that there are 3 possible functioning
 1017 settings:

- 1018 • **1:** the match window is entirely contained after the trigger signal,
- 1019 • **2:** the match window overlaps the trigger signal, or
- 1020 • **3:** the match window is entirely contained before the trigger signal as dis-
 1021 played on Figure A.2.

1022 In both the first and second cases, the sum of the window width and of the
 1023 offset can be set to a maximum of 40 clocks, which corresponds to 1 μ s. Evidently,
 1024 the offset can be negative, allowing for a longer match window, with the constraint
 1025 of having the window ending at most 1 μ s after the trigger signal. In the third case,
 1026 the maximum negative offset allowed is of 2048 clocks (12 bit) corresponding to

1027 51.2 μ s, the match window being strictly smaller than the offset. In the case of
1028 GIF++, the choice has been made to use this last setting by delaying the trigger
1029 signal. During the studies performed in GIF++, both the efficiency of the RPCs,
1030 probed using a muon beam, and the noise or gamma background rate are moni-
1031 tored. The extra search and reject margins are left unused.
1032 To probe the efficiency of RPC detectors, the trigger time tag is provided by the
1033 coïncidence of scintillators when a bunch of muons passes through GIF++ area is
1034 used to trigger the data acquisition. For this measurement, it is useful to reduce the
1035 match window width only to contain the muon information. Indeed, the delay in
1036 between a trigger signal and the detection of the corresponding muon in the RPC
1037 being very contant (typically a few tens of ns due to jitter and cable length), the
1038 muon signals are very localised in time. Thus, due to a delay of approximalety
1039 325 ns in between the muons and the trigger, the settings where chosen to have a
1040 window width of 24 clocks (600 ns) centered on the muon peak thanks to a nega-
1041 tive offset of 29 clocks (725 ns).
1042 On the otherhand, monitoring the rates don't require for the DAQ to look at a
1043 specific time window. It is important to integrate enough time to have a robust
1044 measurement of the rate as the number of hits per time unit. The triggerring sig-
1045 nal is provided by a pulse generator at a frequency of 300 Hz to ensure that the
1046 data taking occurs in a random way, with respect to beam physics, to probe only
1047 the irradiation spectrum on the detectors. The match window is set to 400 clocks
1048 (10 μ s) and the negative offset to 401 clocks as it needs to exceed the value of the
1049 match window.

1050

1051 *Source Code A.1: Description of C++ object v1190a.*

```

class v1190a
{
    private :
        long             Handle;
        vector<Data32>   Address;
        CVDataWidth      DataWidth;
        CVAddressModifier AddressModifier;

    public:

        v1190a(long handle, IniFile *inifile, int ntdcs);
        ~v1190a();
        Data16 write_op_reg(Data32 address, int code, string error);
        Data16 read_op_reg(Data32 address, string error);
        void Reset(int ntdcs);
        void Clear(int ntdcs);
        void TestWR(Data16 value,int ntdcs);
        void CheckTDCStatus(int ntdcs);
        void CheckCommunication(int ntdcs);
        void SetTDCTestMode(Data16 mode,int ntdcs);
        void SetTrigMatching(int ntdcs);
        void SetTrigTimeSubtraction(Data16 mode,int ntdcs);
        void SetTrigWindowWidth(Uint windowHeight,int ntdcs);
        void SetTrigWindowOffset(Uint windowOffset,int ntdcs);
        void SetTrigSearchMargin(Uint searchMargin,int ntdcs);
        void SetTrigRejectionMargin(Uint rejectMargin,int ntdcs);
        void GetTrigConfiguration(int ntdcs);
        void SetTrigConfiguration(IniFile *inifile,int ntdcs);
        void SetTDCDetectionMode(Data16 mode,int ntdcs);
        void SetTDCResolution(Data16 lsb,int ntdcs);
        void SetTDCDeadTime(Data16 time,int ntdcs);
        void SetTDCHeadTrailer(Data16 mode,int ntdcs);
        void SetTDCEventSize(Data16 size,int ntdcs);
        void SwitchChannels(IniFile *inifile,int ntdcs);
        void SetIRQ(Data32 level, Data32 count,int ntdcs);
        void SetBlockTransferMode(Data16 mode,int ntdcs);
        void Set(IniFile *inifile,int ntdcs);
        void CheckStatus(CVErrorCodes status) const;
        int ReadBlockD32(Uint tdc, const Data16 address,
                         Data32 *data, const Uint words, bool ignore_berr);
        Uint Read(RAWData *DataList,int ntdcs);
    };

```

1053 The v1190a object, defined in the DAQ software as in Source Code A.1, offers
 1054 the possibility to concatenate all TDCs in the readout setup into a single object con-
 1055 taining a list of hardware addresses (addresses to access the TDCs' buffer through
 1056 the VME crate) and each constructor and method acts on the list of TDCs.

1057

1058 A.4.2 DataReader

1059 Enabled thanks to v1190a::SetBlockTransferMode(Data16 mode, int ntdcs),
 1060 the data transfer is done via Block Transfer (BLT). Using BLT allows to tranfer a
 1061 fixed number of events called a *block*. This is used together with an Almost Full

1062 Level (AFL) of the TDCs' output buffers, defined through `v1190a::SetIRQ(Data32`
 1063 `level, Data32 count, int ntdcs)`. This AFL gives the maximum amount of
 1064 32735 words (16 bits, corresponding to the depth of a TDC output buffer) that
 1065 can written in a buffer before an Interrupt Request (IRQ) is generated and seen by
 1066 the VME Bridge, stopping the data acquisition to transfer the content of each TDC
 1067 buffers before resuming. For each trigger, 6 words or more are written into the
 1068 TDC buffer:

- 1069 • **a global header** providing information of the event number since the begin-
 1070 ning of the data acquisition,
- 1071 • **a TDC header,**
- 1072 • **the TDC data** (*if any*), 1 for each hit recorded during the event, providing
 1073 the channel and the time stamp associated to the hit,
- 1074 • **a TDC error** providing error flags,
- 1075 • **a TDC trailer,**
- 1076 • **a global trigger time tag** that provides the absolute trigger time relatively
 1077 to the last reset, and
- 1078 • **a global trailer** providing the total word count in the event.

1079 As previously described in Section 4.4.3, CMS RPC FEEs provide us with
 1080 100 ns long LVDS output signals that are injected into the TDCs' input. Any
 1081 avalanche signal that gives a signal above the FEEs threshold is thus recorded by
 1082 the TDCs as a hit within the match window. Each hit is assigned to a specific TDC
 1083 channel with a time stamp, with a precision of 100 ps. The reference time, $t_0 = 0$,
 1084 is provided by the beginning of the match window. Thus for each trigger, coming
 1085 from a scintillator coincidence or the pulse generator, a list of hits is stored into
 1086 the TDCs' buffers and will then be transferred into a ROOT Tree.

1087 When the BLT is used, it is easy to understand that the maximum number of
 1088 words that have been set as ALF will not be a finite number of events or, at least,
 1089 the number of events that would be recorded into the TDC buffers will not be a
 1090 multiple of the block size. In the last BLT cycle to transfer data, the number of
 1091 events to transfer will most probably be lower than the block size. In that case, the
 1092 TDC can add fillers at the end of the block but this option requires to send more
 1093 data to the computer and is thus a little slower. Another solution is to finish the
 1094 transfer after the last event by sending a bus error that states that the BLT reached
 1095 the last event in the pile. This method has been chosen in GIF++.

1097 Due to irradiation, an event in GIF++ can count up to 300 words per TDC. A
 1098 limit of 4096 words (12 bits) has been set to generate IRQ which represent from
 1099 14 to almost 700 events depending on the average of hits collected per event. Then

1101 the block size has been set to 100 events with enabled bus errors. When an AFL
 1102 is reached for one of the TDCs, the VME bridge stops the acquisition by sending
 1103 a BUSY signal.

1104
 1105 The data is then transferred one TDC at a time into a structure called `RAWData`
 1106 (Source Code A.2).

1107

1108 *Source Code A.2: Description of data holding C++ structure `RAWData`.*

```
1109 struct RAWData{
1110     vector<int>           *EventList;
1111     vector<int>           *NHitsList;
1112     vector<int>           *QFlagList;
1113     vector<vector<int>>   *ChannelList;
1114     vector<vector<float>> *TimeStampList;
1115 };
```

1116 In order to organize the data transfer and the data storage, an object called
 1117 `DataReader` was created (Source Code A.3). On one hand, it has `v1718` and `v1190a`
 1118 objects as private members for communication purposes, such as VME modules
 1119 settings via the configuration file `*iniFile` or data read-out through `v1190a::Read()`
 1120 and on the other hand, it contains the structure `RAWData` that allows to organise the
 1121 data in vectors reproducing the tree structure of a ROOT file.

1122

1123 *Source Code A.3: Description of C++ object `DataReader`.*

```
1124 class DataReader
1125 {
1126     private:
1127         bool      StopFlag;
1128         IniFile *iniFile;
1129         Data32  MaxTriggers;
1130         v1718   *VME;
1131         int      nTDCs;
1132         v1190a  *TDCs;
1133         RAWData TDCData;
1134
1135     public:
1136         DataReader();
1137         virtual ~DataReader();
1138         void      SetIniFile(string inifilename);
1139         void      SetMaxTriggers();
1140         Data32  GetMaxTriggers();
1141         void      SetVME();
1142         void      SetTDC();
1143         int      GetQFlag(Uint it);
1144         void      Init(string inifilename);
1145         void      FlushBuffer();
1146         void      Update();
1147         string  GetFileName();
1148         void      WriteRunRegistry(string filename);
1149         void      Run();
1150 };
```

1119 Each event is transferred from `TDCData` and saved into branches of a ROOT
 1120 `TTree` as 3 integers that represent the event ID (`EventCount`), the number of hits
 1121 read from the TDCs (`nHits`), and the quality flag that provides information for any
 1122 problem in the data transfer (`qflag`), and 2 lists of `nHits` elements containing the
 1123 fired TDC channels (`TDCCh`) and their respective time stamps (`TDCTS`), as presented
 1124 in Source Code A.4. The ROOT file file is named using information contained
 1125 into the configuration file, presented in section A.5.2. The needed information is
 1126 extracted using method `DataReader::GetFileName()` and allow to build the out-
 1127 put filename format `ScanXXXXXX_HVX_DAQ.root` where `ScanXXXXXX` is a
 1128 6 digit number representing the scan number into GIF++ database and HVX the HV
 1129 step within the scan that can be more than a single digit. An example of ROOT
 1130 data file is provided with Figure A.3.

1131

1132 *Source Code A.4: Highlight of the data transfer and organisation within
 1132 `DataReader::Run()` after the data has been collected into `TDCData`.*

```
RAWData TDCData;
TFile *outputFile = new TFile(outputFileName.c_str(), "recreate");
TTree *RAWDataTree = new TTree("RAWData", "RAWData");

int EventCount = -9;
int nHits = -8;
int qflag = -7;
vector<int> TDCCh;
vector<float> TDCTS;

RAWDataTree->Branch("EventNumber", &EventCount, "EventNumber/I");
RAWDataTree->Branch("number_of_hits", &nHits, "number_of_hits/I");
RAWDataTree->Branch("Quality_flag", &qflag, "Quality_flag/I");
RAWDataTree->Branch("TDC_channel", &TDCCh);
RAWDataTree->Branch("TDC_TimeStamp", &TDCTS);

//...
//Here read the TDC data using v1190a::Read() and place it into
//TDCData for as long as you didn't collect the requested amount
//of data.
//...

for(Uint i=0; i<TDCData.EventList->size(); i++) {
    EventCount = TDCData.EventList->at(i);
    nHits = TDCData.NHitsList->at(i);
    qflag = TDCData.QFlagList->at(i);
    TDCCh = TDCData.ChannelList->at(i);
    TDCTS = TDCData.TimeStampList->at(i);
    RAWDataTree->Fill();
}
```

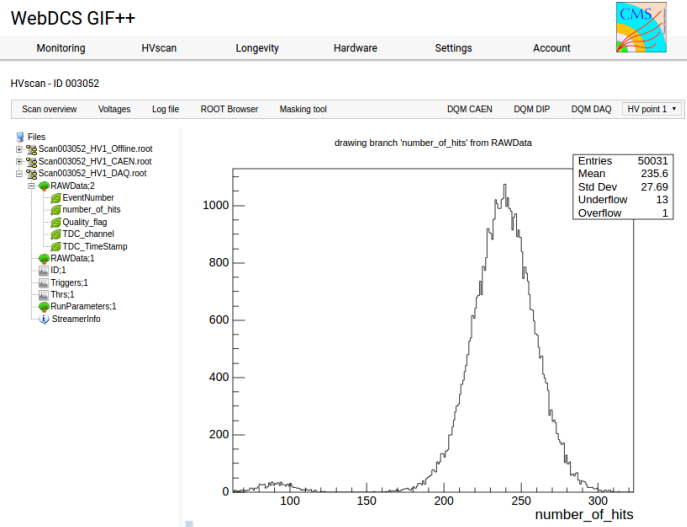


Figure A.3: Structure of the ROOT output file generated by the DAQ. The 5 branches (EventNumber, number_of_hits, Quality_flag, TDC_channel and TDC_TimeStamp) are visible on the left panel of the ROOT browser. On the right panel is visible the histogram corresponding to the variable nhits. In this specific example, there were approximately 50k events recorded to measure the gamma irradiation rate on the detectors. Each event is stored as a single entry in the TTree.

1134 A.5 Communications

1135 To ensure data readout and dialog in between the machine and the TDCs or in
 1136 between the webDCS and the DAQ, different communication solutions were used.
 1137 First of all, it is important to have a module to allow the communication in between
 1138 the TDCs and the computer from which the DAQ operates. When this communica-
 1139 tion is effective, shifters using the webDCS to control data taking can thus send
 1140 instructions to the DAQ.

1141

1142 A.5.1 V1718 USB Bridge

1143 In the previous section, the data transfer has been discussed. The importance of
 1144 the `v1718` object (Source Code A.5), used as private member of `DataReader`,
 1145 was not explicated. VME master modules are used for communication purposes
 1146 as they host the USB port that connects the powered crate buffer to the com-
 1147 puter where the DAQ is installed. From the source code point of view, this ob-
 1148 ject is used to control the communication status, by reading the returned error
 1149 codes with `v1718::CheckStatus()`, or to check for IRQs coming from the TDCs
 1150 through `v1718::CheckIRQ()`. Finally, to ensure that triggers are blocked at the

1151 hardware level, a NIM pulse is sent out of one of the 5 programmable outputs
 1152 (`v1718::SendBUSY()`) to the VETO of the coincidence module where the trigger
 1153 signals originate from. As long as this signal is ON, no trigger can reach the TDCs
 1154 anymore.

1155

Source Code A.5: Description of C++ object v1718.

```
1156
1157 class v1718{
    private:
        int Handle;
        Data32 Data;           // Data
        CVIRQLevels Level;     // Interrupt level
        CVAddressModifier AM;   // Addressing Mode
        CVDataWidth dataSize;  // Data Format
        Data32 BaseAddress;    // Base Address

    public:
        v1718(IniFile *iniFile);
        ~v1718();
        long GetHandle(void) const;
        int SetData(Data16 data);
        Data16 GetData(void);
        int SetLevel(CVIRQLevels level);
        CVIRQLevels GetLevel(void);
        int SetAM(CVAddressModifier am);
        CVAddressModifier GetAM(void);
        int SetDatasize(CVDataWidth datasize);
        CVDataWidth GetDataSize(void);
        int SetBaseAddress(Data16 baseaddress);
        Data16 GetBaseAddress(void);
        void CheckStatus(CVErrorCodes status) const;
        bool CheckIRQ();
        void SetPulsers();
        void SendBUSY(BusyLevel level);
};
```

1158 A.5.2 Configuration file

1159 The DAQ software takes as input a configuration file written using INI standard [13].
 1160 This file is partly filled with the information provided by the shifters when starting
 1161 data acquisition using the webDCS, as shown by Figure A.4. This information is
 1162 written in section `[General]` and will later be stored in the ROOT file that con-
 1163 tains the DAQ data as can be seen from Figure A.3. Indeed, another `TTree` called
 1164 `RunParameters` as well as the 2 histograms `ID`, containing the scan number, start
 1165 and stop time stamps, and `Triggers`, containing the number of triggers requested
 1166 by the shifter, are available in the data files. Moreover, `ScanID` and `HV` are then used
 1167 to construct the file name thanks to the method `DataReader::GetFileName()`.

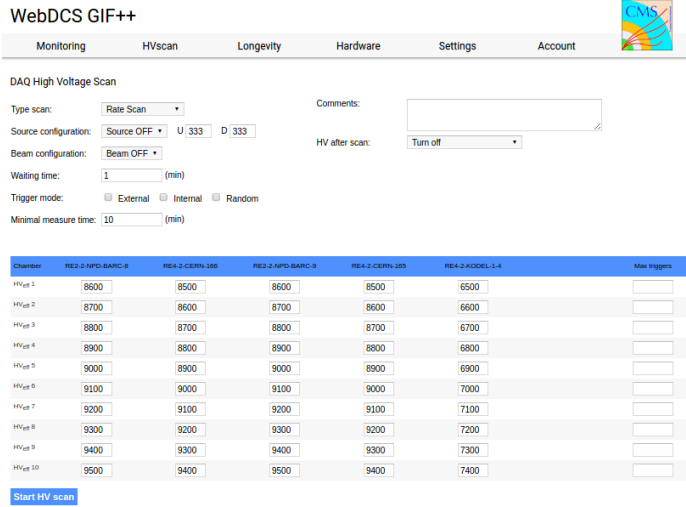


Figure A.4: WebDCS DAQ scan page. On this page, shifters need to choose the type of scan (Rate, Efficiency or Noise Reference scan), the gamma source configuration at the moment of data taking, the beam configuration, and the trigger mode. These information will be stored in the DAQ ROOT output. Are also given the minimal measurement time and waiting time after ramping up of the detectors is over before starting the data acquisition. Then, the list of HV points to scan and the number of triggers for each run of the scan are given in the table underneath.

1168 The rest of the information is written beforehand in the configuration file tem-
 1169 plate, as explicited in Source Code A.6, and contains the hardware addresses to
 1170 the differents VME modules in the setup as well as settings for the TDCs. As the
 1171 TDC settings available in the configuration file are not supposed to be modified, an
 1172 improvement would be to remove them from the configuration file and to hardcode
 1173 them inside of the DAQ code itself or to place them into a different INI file that
 1174 would host only the TDC settings to lower the probability for a bad manipulation
 1175 of the configuration file that can be modified from one of webDCS' menus.

1176

Source Code A.6: INI configuration file template for 4 TDCs. In section [**General**], the number of TDCs is explicited and information about the ongoing run is given. Then, there are sections for each and every VME modules. There buffer addresses are given and for the TDCs, the list of channels to enable is given. Finally, in section [**TDCSettings**], a part of the TDC settings are given.
 1177

```

[General]
TdcS=4
ScanID=$scanid
HV=$HV
RunType=$runtype
MaxTriggers=$maxtriggers
Beam=$beam
[VMEInterface]
Type=V1718
BaseAddress=0xF0000
Name=VmeInterface
[TDC0]
Type=V1190A
BaseAddress=0x00000000
Name=Tdc0
StatusA0-15=1
StatusA16-31=1
StatusB00-15=1
StatusB16-31=1
StatusC00-15=1
StatusC16-31=1
StatusD00-15=1
StatusD16-31=1
[TDC1]
Type=V1190A
BaseAddress=0x11110000
Name=Tdc1
StatusA0-15=1
StatusA16-31=1
StatusB00-15=1
StatusB16-31=1
StatusC00-15=1
StatusC16-31=1
StatusD00-15=1
StatusD16-31=1
[TDC2]
1178 Type=V1190A
BaseAddress=0x22220000
Name=Tdc2
StatusA0-15=1
StatusA16-31=1
StatusB00-15=1
StatusB16-31=1
StatusC00-15=1
StatusC16-31=1
StatusD00-15=1
StatusD16-31=1
[TDC3]
Type=V1190A
BaseAddress=0x44440000
Name=Tdc3
StatusA0-15=1
StatusA16-31=1
StatusB00-15=1
StatusB16-31=1
StatusC00-15=1
StatusC16-31=1
StatusD00-15=1
StatusD16-31=1
[TDCSettings]
TriggerExtraSearchMargin=0
TriggerRejectMargin=0
TriggerTimeSubtraction=0b1
TdcDetectionMode=0b01
TdcResolution=0b10
TdcDeadTime=0b00
TdcHeadTrailer=0b1
TdcEventSize=0b1001
TdcTestMode=0b0
BLTMode=1

```

1179 A.5.3 WebDCS/DAQ intercommunication

1180 When shifters send instructions to the DAQ via the configuration file, it is the web-
 1181 DCS itself that gives the start command to the DAQ and then the 2 softwares use
 1182 inter-process communication through file to synchronise themselves. This com-
 1183 munication file is represented by the variable `const string __runstatuspath`.
 1184 On one side, the webDCS sends commands or status that are readout by the DAQ:

- 1185 • INIT, status sent when launching a scan and read via function `CtrlRunStatus(...)`,

- 1186 • START, command to start data taking and read via function `CheckSTART()`,
- 1187 • STOP, command to stop data taking at the end of the scan and read via
1188 function `CheckSTOP()`, and
- 1189 • KILL, command to kill data taking sent by user and read via function `CheckKILL()`

1190 and on the other, the DAQ sends status that are controled by the webDCS:

- 1191 • DAQ_RDY, sent with `SendDAQReady()` to signify that the DAQ is ready to
1192 receive commands from the webDCS,
- 1193 • RUNNING, sent with `SendDAQRunning()` to signify that the DAQ is taking
1194 data,
- 1195 • DAQ_ERR, sent with `SendDAQError()` to signify that the DAQ didn't receive
1196 the expected command from the webDCS or that the launch command didn't
1197 have the right number of arguments,
- 1198 • RD_ERR, sent when the DAQ wasn't able to read the communication file,
1199 and
- 1200 • WR_ERR, sent when the DAQ wasn't able to write into the communication
1201 file.

1202 **A.5.4 Example of inter-process communication cycle**

1203 Under normal conditions, the webDCS and the DAQ processes exchange com-
1204 mands and status via the file hosted at the address `__runstatuspath`, as explained
1205 in subsection A.5.3. An example of cycle is given in Table A.1. In this example,
1206 the steps 3 to 5 are repeated as long as the webDCS tells the DAQ to take data.
1207 A data taking cycle is the equivalent as what is called a *Scan* in GIFT++ jargon,
1208 referring to a set a runs with several HV steps. Each repetition of steps 3 to 5 is
1209 then equivalent to a single *Run*.

1210
1211 At any moment during the data taking, for any reason, the shifter can decide
1212 that the data taking needs to be stopped before it reached the end of the scheduled
1213 cycle. Thus at any moment on the cycle, the content of the inter-process commu-
1214 nication file will be changed to KILL and the DAQ will shut down right away. The
1215 DAQ checks for KILL signals every 5s after the TDCs configuration is over. So
1216 far, the function `CheckKILL()` has been used only inside of the data taking loop
1217 of method `DataReader::Run()` and thus, if the shifter decides to KILL the data
1218 taking during the TDC configuration phase or the HV ramping in between 2 HV
1219 steps, the DAQ will not be stopped smoothly and a *force kill* command will be
1220 sent to stop the DAQ process that is still awake on the computer. Improvements
1221 can be brought on this part of the software to make sure that the DAQ can safely
1222 shutdown at any moment.

1223

step	actions of webDCS	status of DAQ	__runstatuspath
1	launch DAQ ramp voltages ramping over wait for currents stabilization	readout of IniFile configuration of TDCs	INIT
2		configuration done send DAQ ready wait for START signal	DAQ_RDY
3	waiting time over send START		START
4	wait for run to end monitor DAQ run status	data taking ongoing check for KILL signal	RUNNING
5		run over send DAQ_RDY wait for next DCS signal	DAQ_RDY
6	ramp voltages ramping over wait for currents stabilization		DAQ_RDY
3	waiting time over send START		START
4	wait for run to end monitor DAQ run status	update IniFile information data taking ongoing check for KILL signal	RUNNING
5		run over send DAQ_RDY wait for next DCS signal	DAQ_RDY
7	send command STOP	DAQ shuts down	STOP

Table A.1: Inter-process communication cycles in between the webDCS and the DAQ through file string signals.

¹²²⁴ **A.6 DAQ algorithm overview**

¹²²⁵ **A.7 Software export**

B

1226

1227

Details on the online analysis package

1228

B.1 Introduction

1229

insert text here

C

1230

1231

1232

Structure of the hybrid simulation software

1233

C.1 Introduction

1234

insert text here...

